2021

Design of Lower Legs of Mithra, a High-Performance Backdrivable Humanoid Robot

Drake Taylor

Design of Lower Legs of Mithra, a High-Performance Backdrivable Humanoid Robot

_____

A Thesis

Presented to

the Faculty of the Daniel Felix Ritchie School of Engineering and Computer Science

University of Denver

_____

In Partial Fulfillment

of the Requirements for the Degree

Master of Science

_____

by

Drake Taylor

November 2021

Advisor: Dr. Siavash Rezazadeh

Author: Drake Taylor
Title: Design of Lower Legs of Mithra, a High-Performance Backdrivable Humanoid Robot
Advisor: Dr. Siavash Rezazadeh
Degree Date: November 2021

Abstract

This thesis presents the design of the knee and ankle of Mithra, a new humanoid robot that aims to be an energy-efficient and highly agile machine. Mithra makes use of new optimization metrics for legged robots to develop a system capable of mimicking human movement. A series of low-impedance, high-torque actuator systems were developed with the goal of creating lightweight, powerful, and robust motion. The structure of Mithra's legs mimics the human structure in leg segment length and weight proportions. Detailed design and analysis were conducted in order to allow Mithra to be a robust and maintainable system. Mithra will serve as a human movement controls research platform and is mechanically capable of running at 3 m/s.

Acknowledgements

I would like to extend my deepest gratitude to my research advisor, Dr. Siavash Rezazadeh; without his guidance and knowledge, this research would not have been possible. Additionally, I would like to thank Chathura Semasinghe for developing Mithra with me and always being a reliable friend and source of knowledge. I am deeply grateful to Justin Huff for his contribution to my manufacturing education and contributions to Mithra. I wish to acknowledge the unrelenting support, guidance, and love of my parents, Thomas and Renee Taylor; grandparents: Cynthia and James Griffin; my partner, Sarah Grossi: and my closest friend, Ricardo Centeno.

Table of Contents

List of Figures

List of Tables

Chapter One: Introduction

Humans have always been intrigued by creating something in their image, and robots have long been the focus of that longing. Robots are seen drawn and dreamed up in ancient cultures, and while it is complicated to create technology, most developments have not evaded us as the humanoid robot has. Planes, cars, buildings, even computers have become streamlined, and advancements are constantly being made. However, humanoid robots still do not have many of the capabilities that humans do. To match the forces, stability, and fluidity of human movement is a challenge limited by materials, manufacturing methods, computing power, battery power, actuators, and control methods. This difficulty is primarily because of how incredible the human body truly is. The best way to close this gap in robotic performance is to develop new theories and technologies and test them on new humanoid robots. Seeing that there is a current gap of energy efficiency combined with agility in humanoid robotics, we designed Mithra. Mithra will serve as a mechanical platform for controls research. It aims to run at 3 m/s while kinematically mimicking all the movements of a human leg. Mithra aims to be an energy-efficient humanoid with high agility and strength by utilizing low-impedance high-torque actuators and a lightweight design.

1.1 Literature Review

In 1983, a revolutionary moving robot was created: a one-legged 3D hopper. The hopper consisted of a large platform with a pneumatic 2 DOF hip and linear actuator powered by compressed air acting as a pogo stick, as it can be seen in Figure 1. Standing 1100 mm tall and weighing 17.3 kg, the robot was one of the first to show that balance can be achieved in movement by using a simple control system[1]. The control system was split into three parts: forward speed, body altitude, and hopping height. By developing simple systems, they could take the 2D control to 3D and manage small disturbances while demonstrating a maximum running speed of 2.2 m/s [2]. The hopper was an ideal first step in exploring human movement, as it offered a majorly simplified view of human movement and robotics. Robots that expanded on Raibert's hopper needed to add several steps of complexity to achieve a humanlike gait. The key changes necessary include adding a second leg, more DOF (like knee flexion), and actuators that could be controlled much easier.

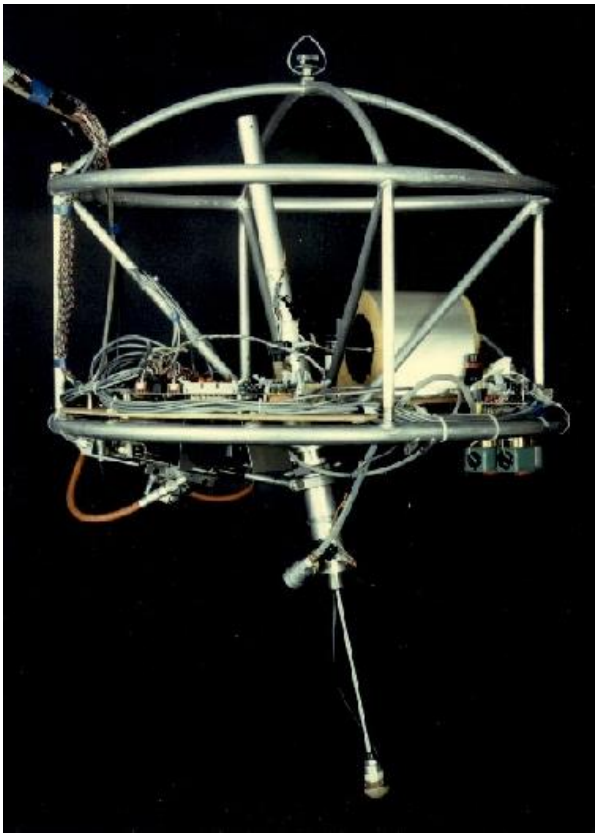

Figure 1: Raibert's One Legged Hopper[3]

Tad McGeer at Simon Fraser University took a different approach to develop a walking robot in 1990, designing it so it does not need to be controlled at all. Inspired by toys that can walk on their own, McGeer created a passive walking robot. This is a type of bipedal robot that enables walking with only the force of gravity driving them. Because they are designed with walking as a natural mode, the only input needed for motion is a small downward slope to compensate for the energy loss during impacts. [4]. The robot is laterally balanced by having two outer legs that act as crutches to swing the middle legs forward, and then the middle legs will hold the robot as the outer legs swing forward. These passive walkers were a huge push forward and inspired many robots.

Figure 2: Cornell Ranger[5]

The Cornell Ranger was heavily inspired by the passive walkers and took them a few steps farther by adding actuators. With a simple laterally balanced design, like Mcgeer's passive walker, the goal of Ranger was to move as efficiently as possible. In 2011 Ranger set an unofficial record for walking 40.5 miles untethered. Designed with two outer legs and two inner legs (Figure 2), it can walk on flat ground using little energy just like the passive walkers. Its motion is propelled by two motors, one motor is connected to the outer legs, and one is connected to the inner legs, allowing them to move in sync [6]. Ranger's passive dynamics allow it to have a Total Cost of Transport (TCOT) of 0.28. TCOT details the amount of energy per mass that it takes a robot to move, it is a general gauge of energy efficiency. Humans also have a TCOT of around .28 and in contrast, a fully actuated humanoid like ASIMO is estimated to have a TCOT of 3.5 [6]. Ranger took passive walkers to new limits, but still had many shortcomings. For example, slight changes in ground height could easily disrupt its movement and lead to falling. Ranger was also limited by its DOF, its legs only swung in one direction. These

are areas in which future robots attempted improve on by making use of the spring-mass model.

Figure 3: ATRIAS

The spring-mass model presents a philosophy similar to that of passive walkers, designing a system that uses cleverly placed passive elements (springs) so that motion occurs naturally. A good example of a robot that highlights this idea is ATRIAS (Figure 3). Designed with the spring-mass model as its template, ATRIAS is underactuated and finds its walking stability as a partially natural mode. On each leg, two motors control sagittal plane motion, and one controls abduction/adduction. The sagittal plane motors are placed in series with two low stiffness Leaf springs on each leg, pictured in Figure 4. This method of actuation is referred to as Series Elastic Actuation. ATRIAS utilized this structure with two four-bar linkages, one for full leg flexion and one for knee flexion.

ATRIAS demonstrates that the capabilities of robots can be extended by designing them to leverage their natural dynamics for responding to inputs, which can also improve energy efficiency[7].

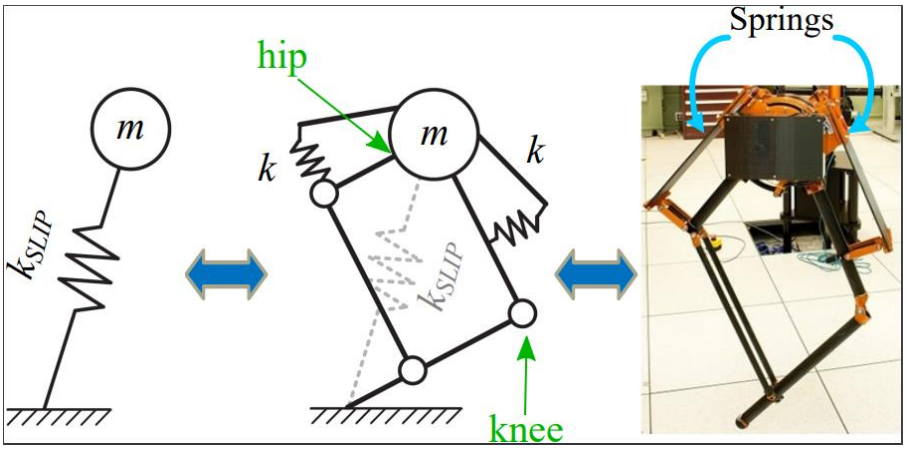

Figure 4: Design of ATRIAS leg mechanism based on spring-mass model (Figure courtesy of Siavash Rezazadeh)

ATRIAS was designed to embody the dynamics of a template of biological walking, but Kenshiro and Kengoro took another route to address the problem by closely mimicking the human biomechanics. The Kenshiro and Kengoro robots, developed by JSK Labs, both employ a musculoskeletal design unlike anything in other humanoid robots. They are pictured in Figure 5 and Figure 6, respectively. Kenshiro was developed in 2012, and a driving factor behind its design was to mimic the human bone and muscle structure. The authors state that robots designed with traditional actuators, while easier to control, do not adequately imitate the human body and human movement [8]. Kenshiro avoided this by having redundant tendons and muscles as well as a bone structure that mimics humans. Kenshiro stands at 1580 mm tall, with a weight of 50 kg, and has 100 actuators allowing for 64 DOF (except for hands). Kenshiro sets itself apart with humanlike bone shapes that are manufactured from Metal SLS (Selective Laser

Sintering), CFRP (carbon fiber reinforced plastic), and Aluminum casting and cutting work. A sturdy frame is positioned on a spring and planar muscle mechanism that allows for a stable core section to mimic humans [9].

Figure 5: Kenshiro in motion(© JSK Robotics Lab, The University of Tokyo)

Figure 6: Kengoro full body view(© JSK Robotics Lab, The University of Tokyo)

Kengoro was a significant upgrade using the lessons learned from Kenshiro, finished in 2016. What is particularly interesting about Kengoro is that the legs are each 48 DOF, with 3 for the hip, 2 for the knee, 3 for the ankle, and 16 for the foot. This is in sharp contrast to most humanoid robots with 6 to 7 DOF. While this method has the advantage of being biologically accurate, it comes at the cost of controllability. The control systems are still being worked on because of the complexity of muscles and their non-linearity. Their current research is designing a software system capable of controlling and moving Kengoro in a humanlike manner. It is capable of balancing and moving, but human gaits are still out of reach [10]**.**

Most other current humanoid robots employ much simpler mechanics to create a more controllable robot. A notable example of this is ASIMO. ASIMO is an advanced moving humanoid robot that is the culmination of robotic development performed by

Honda since 1986. The E series was experimental, developed with the purpose of trying different things as the field was scarce at the time. All of Honda's robots were only humanoid from the hips down until they announced P1 in 1993. The prototype series started including arms, and by 2000 ASIMO was introduced. Each leg of ASIMO has 6 DOF and a waist with 2 DOF comes on top of them. It uses harmonic drives for its actuation and is mostly made of a magnesium alloy. Harmonic gears are a type of actuator system with the ability to reach high gear ratios with little backlash. The ankle uses a parallel crank rocker mechanism along the Shank to allow for pitch and roll movement. This off-axis parallel structure allows for the overall leg inertia to be lowered by moving the actuator as far up the Shank as possible [11].

The Humanoid Robotics Project (HRP) is another group that is at the forefront of robotics technology and has created eight humanoid robots that serve various purposes and have improved over the past years. Starting with HRP-1 in 1997, they have been iterating through humanoid robots ever since[12]. Their second robot, HRP-2, was a large advancement in humanoid robotics, pictured in Figure 8, highlighting a highly stylized design and a broad range of capabilities. They aimed to improve the capabilities and weight of their robot with HRP-4 in 2010. Weighing only 39 kg and standing 1510 mm tall, it is much lighter and more powerful than the previous iterations. HRP-4 achieved these goals by utilizing transmission systems that included ball screws, pulley belts, and harmonic gears[13]. While this system was able to output the necessary torques and rotational speed, it has its downsides. Harmonic gears and ball screws create a system that is not backdrivable, hurting overall efficiency. Along with that harmonic drive gears

are already less efficient than other systems, such as, planetary gear systems. This system was improved upon in the next iteration of the HRP family.

Figure 7: HRP-2 (©AIST, KAWADA Robotics)

HRP-5 is their newest iteration in the series and is a heavy-duty humanoid robot weighing 101 kg and standing at 1820 mm tall[14]. It is presented in Figure 8. The main goal of this robot is to work autonomously in hazardous environments and replace the need for human labor. It can carry loads of 13 kg and pick up sheetrock and other strangely shaped objects. In order to enable this, high-torque drive systems were created for each joint, each consisting of one to three motors connected with a pulley. This pulley is then attached to a harmonic drive gear with a further reduction ratio. For example, the knee can put out 922 Nm for torque, and the waist can output 450 Nm in the roll and pitch directions. This design allows most of the weight of hip and knee actuators to be placed off-axis and reduce the distal mass of the legs, but the ankle actuators are placed

on axis at the foot. This mass at the foot is made up for by the strength of the actuators. While the actuators are powerful, this comes at the price of speed. The knee joint can move at a maximum speed of 5.5 rad/s while a human knee joint can move anywhere from 16 to 28.4 rad/s at a maximum speed, depending on flexion or extension[14].

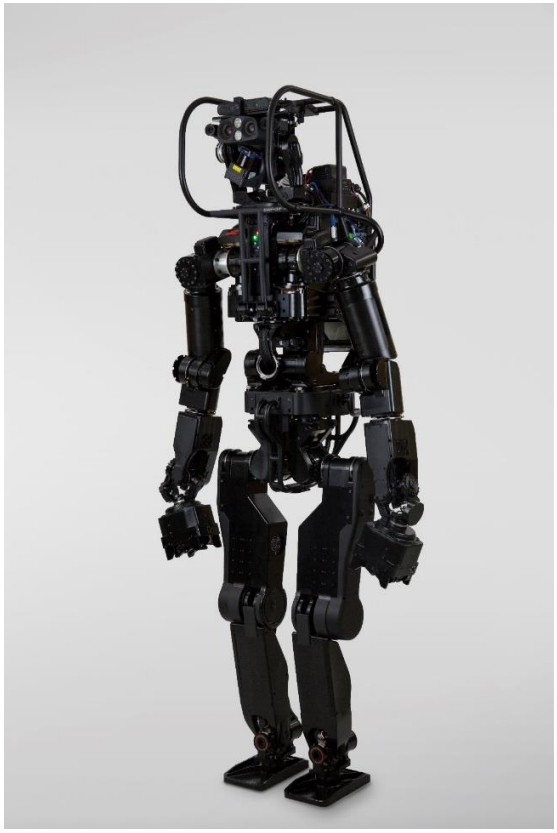

Figure 8: HRP-5 (©AIST)

One of the main competitors to the HRP-5 is TALOS, a series of humanoid robots that aim to be an innovation in industrial humanoids. It is 1750 mm tall with a weight of 95 kg and 32 DOF. Each leg is made up of 6 DOF and is able to output high torques. It uses brushless motors attached to harmonic drives in order to put out high torques at reasonable speeds; these actuators are then attached to a torque sensor to enable precise torque control. TALOS was developed not only to have the movement capabilities of a

human, but even more. It was designed with extra room for the legs to rotate, enabling 40 degrees more rotation than a human hip [15]. TALOS and HRP-5 are both heavy and powerful robots filling in the industrial space of robotics, but robots like Wabian-2R are focused on testing human products with accurate motion.

Figure 9:Wabian-2R (©Atsuo Takanishi Lab., Waseda University)

Wabian-2R is a development from Takanishi Laboratory. It is pictured during walking in Figure 9. Wabian-2R is a 41 DOF robot that was designed to mimic human walking of the elderly and disabled in order to test welfare equipment. Each leg has 6 Degrees of Freedom[16]. It weighs 64 kg and is 1500 mm tall, running on dc servo motors tied to belt reductions and harmonic drive systems. Wabian 2R has two design choices that mimic human movement and allow for several types of walking. The first of

these design choices is a two DOF pelvis. These are redundant DOF that allow for a knee-stretched walking movement. This is a similar design to ASIMO and allows the leg to clear the ground easier while walking and avoid a knee-bent walking gait [17]. This has been adapted into more humanoid robots over time as it is especially useful for allowing the foot to clear the ground easily in the swing phase as well as balance.

Another impressive design implemented into Wabian-2R is the arched compliant foot design (Figure 10). The compliant toe coupled with a high arch works so that at the height of plantarflexion, the foot's arch is pushed outward, acting as a spring, and storing energy for the gait [18]. While research is still being conducted on exactly how a human foot impacts the gait, this design is one step in furthering the understanding of gait dynamics.

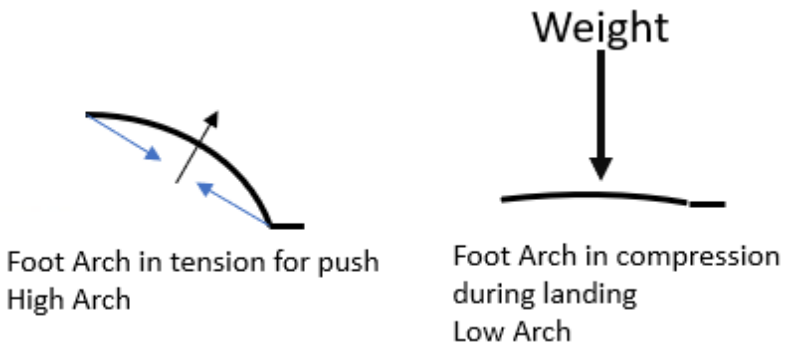

Figure 10: Simplified example of Wabian-2R arched foot

Another humanoid robot that focuses heavily on robust design and gait dynamics is LOLA. LOLA's mechatronic-focused design, along with a specially developed foot, allows it to achieve a humanlike gait. It weighs 60 kg, has a height of 1800 mm, and has 25 DOF. LOLA focuses on its mechatronic design and foot design in order to create a robust humanoid with great acceleration. Every aspect of the design in LOLA is deeply

investigated and optimized. The kinematic structure and final build of Lola is pictured in Figure 11. The link length was decided via dynamics, and it was determined that a lightweight but high rigidity shank was necessary to achieve a proper gait. Connection points, desired outer shape, and the material was all determined and mocked up in CAD. They then used topology optimization to create a lightweight and rigid shape to be cast. This has its disadvantages, such as cost and complexity to make, but it is also a very efficient way to use metal in a design [19].

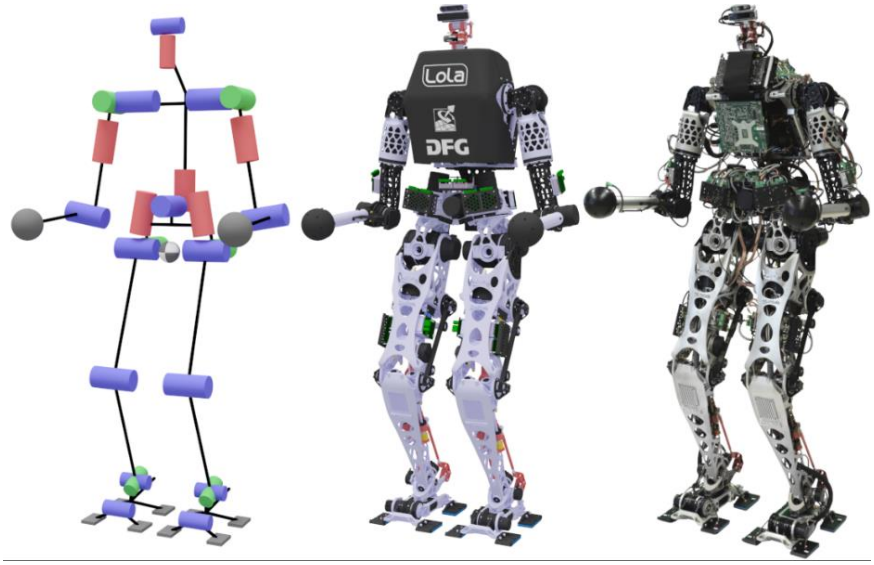

Figure 11: Humanoid robot LOLA, (Figure courtesy of Chair of Applied Mechanics, Technical University of Munich)

The foot is actuated by two slider-crank mechanisms located along the Shank, which allow for 2 DOF-powered movements. This off-axis mechanism, much like that of ASIMO, allows for distal mass to be moved farther up the leg, but it is still below the knee joint [20].

While LOLA puts a sharp lens onto the design of every part, the CogiMon laboratory has focused on creating systems that make robots easier to make and

expanding the possibilities of robotics. The CogiMon (Cognitive Interaction in Motion Laboratory) has created many different robots and developed their own actuators. Their main humanoid is referred to as the CogiMon Humanoid robot. The legs have 6 DOF, and the hip and knee joints take advantage of their TREE actuators to have an on-axis configuration. These actuators allow for easy integration into robotic systems and come with many options for torque outputs and data collection. The ankle, however, is similar to ASIMO and LOLA, with a parallel structure driven by two decoupled TREE actuators just below the knee joint. A primary difference is the type of actuation and joint layout. LOLA uses a UPU (Universal, Prismatic, Universal) layout, while CogiMon uses an RSS (Radial, Spherical, Spherical) layout. The main difference is the nonlinearity of torque distribution depending on ankle angles. With a UPU system, if the ankle is not in a flat position, the torques applied are not exactly equal, but with an RSS system, they are identical no matter what the angle [21]. Figure 12 depicts the basic kinematic layout of the CogiMon ankle, with its shank running along the z axis not pictured. The CogiMon Humanoid robot provides a solid mechanical platform for advancing robotic controls, but robots like the Nimbro-OP2X aim to provide a lightweight controllable robot that comes at a very low price point.

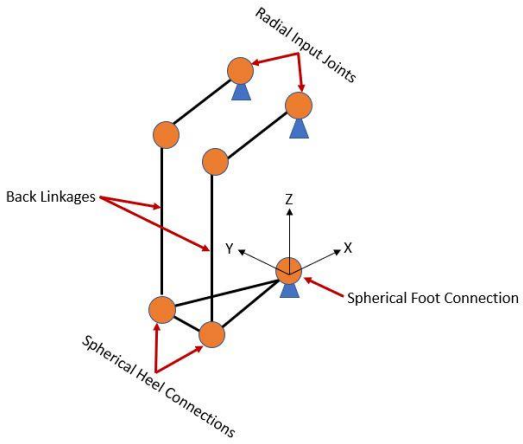

Figure 12: CogiMon ankle kinematic system

Figure 13: Nimbro-OP2X competing in Robocup 2018 (Autonomous Intelligent Systems, University of Bonn, Germany.)

The Nimbro-OP2X was developed in 2018 for the Robocup soccer tournament and is pictured playing in Figure 13. It stands 1350 mm tall with 18 total DOF. Each leg utilizes parallel mechanisms and has 5 DOF. Two four-bar linkages are used, one to drive the knee movement, one to drive ankle pitch, and a serial actuator to drive the ankle roll. Because of its use of 3D printed materials, it weighs only 19 kg. This robot is unique in the fact that the gears are printed as part of the structure. 3D printing gears has several

distinct benefits, such as weight reduction, simple manufacturing, and easily replaceable parts. While it is smaller in scale than other humanoid robots, it displays impressive movement for a completely 3D printed design and its price point of under $35,000 [22][23].

While all the aforementioned robots are extraordinary and all perform to their purpose, Atlas stands above as the best humanoid robot currently functioning. Standing 1500 mm tall and weighing 80 kg Atlas is the most dynamic robot in the world, able to do parkour and even backflips. This is possible by making use of 28 hydraulic actuators that have custom-designed valves to be as light and powerful as possible. Having a large hydraulic tank in the chest allows for the limbs to have significantly lower inertia than other kinematic layouts[24]. While hydraulic actuators currently allow for Atlas to create better motion than most robots, it comes with many disadvantages. Hydraulic actuators are not energy efficient. The TCOT of Atlas is an order of magnitude higher than electrically actuated robots and this makes it best suited for demonstrations currently. Another disadvantage of Atlas is the high customization of parts. These parts allow for the system to work well but come at a high cost.

Mithra aims to improve on aspects where current humanoid robots lack. The first improvement is finding an optimal balance between TCOT and stability/agility. There is an unavoidable trade-off between efficiency and agility. This is evident when comparing passive walkers to full humanoids. While this argument compares two edge cases, it is true for all robots. The high gear ratios used in most robotic actuators, whether harmonic gears or ball screws, lead to lower energy efficiency. An increase in gear ratio brings with

it an increase in joint friction and reflected inertia, which are the main causes for lower efficiency. High impedance actuators also complicate force and impedance control during the stance phase as they add unmodeled dynamics to the system. Mithra was designed with high torque, low impedance actuator systems in order to allow each joint to be easily backdrivable. In addition to stance-phase force control, this approach allows the knee joint to passively move during the swing phase. This passive motion allows for a more energy-efficient gait and simpler controls. Biologically inspired link weights and lengths were designed to help develop a kinematically accurate leg system. Mimicking the kinematics of a human leg was important for many reasons. Firstly, so that Mithra can be used as a platform to further research on humanoid robot controls, and the second reason was so that the design philosophies used could eventually be used in creating exoskeletons and prosthetics. By designing everything proportional to a human body, slight changes to the design philosophy should allow for the controls research and mechanical design to be expanded into wearable robots.

In this thesis the high-level concept design of Mithra will be discussed, and the knee and ankle systems will be closely examined. Chapter 2 will explain the design philosophies and methodologies. Chapter 3 will detail the mechanical requirements for Mithra's motion. This chapter will detail the motor selection, gearbox design, system analysis, and the inverse kinematics of our 2-DOF ankle. Chapter four will conclude the thesis by detailing the results of benchtop testing and validating the inverse kinematics of the ankle mechanism. This chapter will also lay out design improvement suggestions and lessons learned from developing this system.

Chapter Two: Conceptual Design and Performance Objectives

2.1 Kinematic Layouts of Humanoid Robotic Legs

There are four prominent actuator layouts that almost all humanoid robots will fall into; Atlas and Kenshiro/Kengoro are exceptions because of their unique actuator choices of hydraulics and muscle-like actuators, respectively [25]. The kinematic structures are pictured in Figure 14 mentioned in the order that they appear from left to right.

On-Axis Serial: This method involves having the actuators placed exactly at each joint. This method leads to more weight being farther down the leg and has higher inertia because of this. High inertia can lead to positional errors and lower efficiency. Almost all humanoid robots currently use this for the hip and knee configurations as it is a simple way to connect an actuator to a joint. This can be seen in many robots as it is the simplest mechanical construction. For example, in the joints of TALOS.

Off-Axis Serial: Placing the actuators higher up the limb and coupling them to the joint with a lightweight linkage creates an off-axis serial connection, such as a belt. The joints of HRP-5 are an example of this.

Parallel: Either a crank rocker type linkage or linear actuator placed off-axis. This type of actuation can be seen on the ankles of ASIMO.

Mixed Serial/Parallel: A mix of off and on-axis actuation styles that simplifies areas that need little torque, such as the ankle inversion, by placing the actuator directly on the

axis while larger actuators such as the knee are placed higher up the leg to lower the inertia. The Nimbro-OP2X is a notable example of how these methods can be mixed[25].

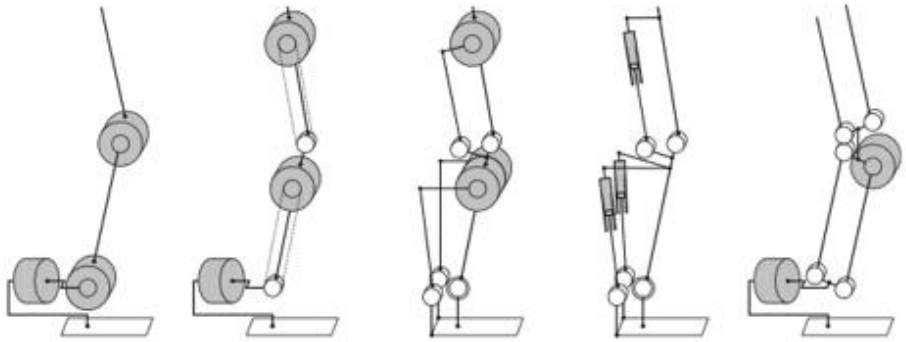

Figure 14: Leg kinematic structures by Gregorz Ficht, Steven Behnke is licensed under CC BY 4.0, http://creativecommons.org/licenses/by/4.0/. [25]

2.2 Mithra's Kinematic Structure, Range of Motion, and Actuator Placement

To accurately replicate human movement, many factors are needed. The first is degrees of freedom. A human leg has many degrees of freedom, but six degrees of freedom (DOF) can capture the main kinematic attributes with sufficient accuracy: three at the hip, one at the knee, and two at the ankle [26]. This is a standard configuration for humanoid robots; the differences between robots comes from where the actuators are placed and whether they make use of parallel or on-axis mechanisms. The basic kinematic layout of Mithra is general for most humanoid robots and follows the form presented in Figure 15.

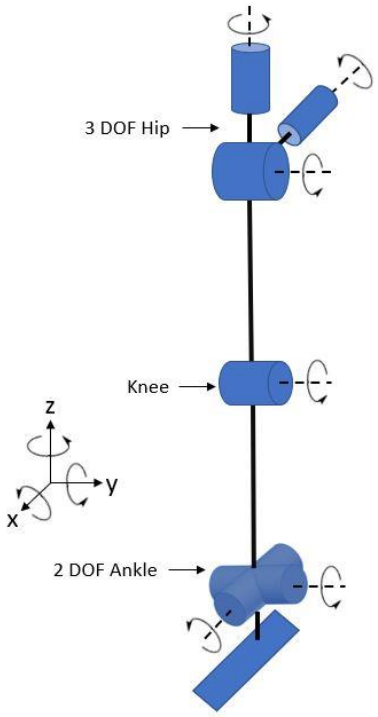

Figure 15: Mithra's basic kinematic structure

For Mithra’s hip, three on-axis actuators are placed with their axes intersecting each other to simulate a spherical joint with actuation. Utilizing an on-axis design simplifies the kinematic analyses and at the same time mimics the human hip joint. The hip is the joint that has the least to gain from utilizing parallel mechanisms. This is because it is located at the base of the leg’s kinematic chain during swing. While the hip is better suited for on-axis actuation, the knee and ankle are the opposite. These joints are farther down the leg, and this means that any mass present creates much higher inertia around the hip. Higher inertias in the leg lead to higher torque requirements for actuators swinging the leg and a greater chance for positioning errors [25]. For this reason, it was imperative that the knee and ankle make use of off-axis parallel mechanisms, as

presented in Figure 16. The original design for Mithra's leg layout is shown in Figure 16, showing the inertia-minimizing placement of actuators with the knee actuator located at the hip joint and the ankle actuator located at the knee joint. While this layout would have been ideal for minimizing distal mass, it was determined that mechanically it would be too difficult to place the knee directly at the hip. The space that each actuator takes up was too large to fit within any reasonable parameters of leg size. By locating the knee actuator mid-thigh, and the ankle actuator at the knee joint, a compromise was made between leg inertia, mechanical simplicity, and optimal leg shape.

There were still some difficulties in placing parallel mechanisms in the leg. Because the leg also needed to have an accurate range of motion for each joint, the designs needed to be specialized, the range of each joint is shown in Table 1. For example, the knee needed to be made so that there was room for the linkage to move 140 degrees with no interference at either end of the mechanism. The ankle having two DOF necessitated two gearboxes and motors to be placed in a small space, so the actuator assembly had to be made wider than desired. Although the ankle actuator is wider than optimal, it is also higher up the leg than most robots have been able to achieve. For example, ASIMO and CogiMon both control their ankles from below the knee joint. While the difference is only a few centimeters, the difference in distal mass is enough to impact the movement of the leg.

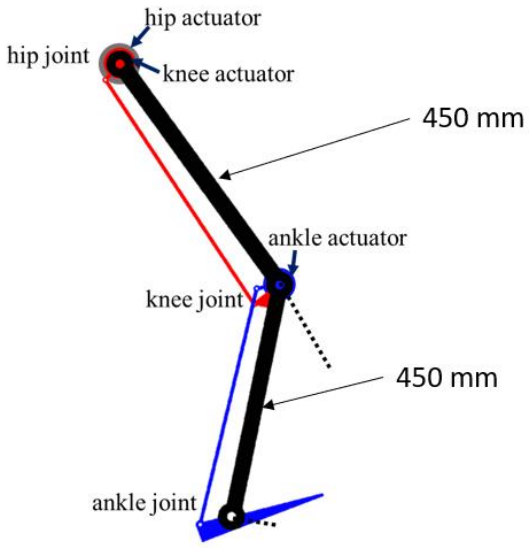

Figure 16: Schematic of leg design (Figure courtesy of Chathura Semasinghe)

Table 1: Human leg ranges of motion and Mithra ranges of motion[26]

Motion	**Human Range(degrees)**	**Mithra Range(degrees)**
Plantarflexion/Dorsiflexion	-40, +20	-42, + 29
Inversion/Eversion	-30,30	-31, +27
Knee Flexion	0, +145	0, +145
Hip Pitch	-120, +10	-120, +10
Hip Roll	-40, + 30	-40, +30
Hip Yaw	-35, + 35	-35, +35

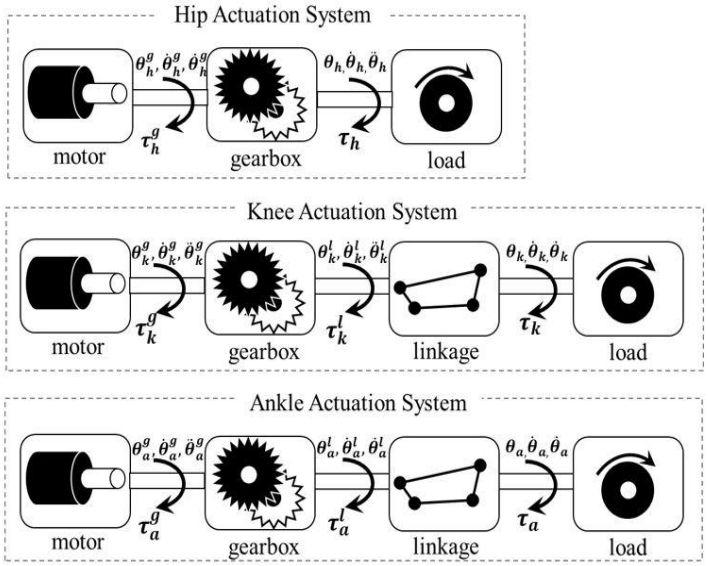

Figure 17:Actuation system flowchart (Figure courtesy of Chathura Semasinghe)

A second key factor considered for Mithra was leg segment lengths; the distance between joints is critical for having a kinematically correct system. The average distance between the joints was considered for an 1800 mm tall human which results in a distance of 450 mm between the ankle and knee joints and 450 mm between the knee joint and hip joint [26]. These lengths were a strict requirement of the design as the motor and actuator optimization for swing dynamics was done using these values. It was also necessary to have a fully actuated design to mimic an extensive range of human locomotion maneuvers, including walking, running, sit-to-stand, stair ascent and descent, turning, and squatting.

2.3 Low-Impedance Actuation

While Mithra could have been designed using springs to add passive compliance during gait cycles, low-impedance actuators were used instead. A low impedance actuator is able to mimic a spring, but with several advantages over a traditional spring.

The first major advantage over a spring is that a low-impedance actuator can mimic varying stiffness values. To replicate this system with springs would make the actuator system bulky and is not suitable for leg-designs. The second major advantage over a spring is ease of control, a spring complicates control for an by increasing the relative degree of the system[27].

Incorporating a low impedance transmission also allows for the leg to have a minimally actuated knee swing and move with less torque from the motors as gravity provides additional torque. There are currently several robots and prosthetics that have used this low impedance approach, but very few humanoid robots have been able to make use of it due to the high torque demands. Notable robots and prosthetics that have used this setup include the MIT Cheetah[28], Cassie [29], and UTD Prosthetic Leg 2[30]. These robots are quadruped and biped, respectively but are both able to take the same advantages from low impedance design.

While there was no specific upper limit for gear ratio in the optimization formulation, it penalized frictional losses and inertias associated with increasing the gear ratio, leading to lower impedance gearboxes. One of the ways that high transmission ratios can affect the performance of robotic systems is through increasing the effect of joint unmodeled dynamics, which can make the control of the system difficult. Simply put, low-impedance actuation allows a system to work as it is ideally modeled. Another set of advantages is energy regeneration and shock absorption [31]. During the swing phase, gravity can pull the shank down and spin the knee motor, allowing energy to be regained in the batteries. With a high impedance system, the motor would need to be

powered during this stage because the high friction causes gravity to have a minimal effect on moving the leg. Along with this, when the foot hits the ground, a low-impedance actuator can be back-driven to absorb the shock and mitigate the impact[31]. This is not only a mechanical benefit as it prolongs the life of the system by reducing part wear, but it also improves the energy efficiency of the system. The ability to react naturally to inputs is vital to the success of this system for another reason: impedance control. Using a low-impedance system the impedance control allows the actuator to react like there is a spring in the system, even when a physical spring is not present. This gives the advantages present in passive robots, without the disadvantage of more complicated controls. The compliancy of the actuators allows for it to strongly favor humanlike trajectories [30].

A last but still important advantage of a low impedance system is the limitation of mechanical noise[30]. Naturally, the less friction and impedance there is, the quieter a system will be. It was important that Mithra be as quiet as possible because as robots become more prevalent in human spaces, their noise has to be considered.

While high impedance systems are less efficient and require more complicated controls, they have historically been one of the only options. Until recently, brushless DC motors were not capable of outputting enough torque at high enough RPMs to allow for low impedance transmissions to be viable [25]. High impedance drives allow for motors with low torque ratings to be utilized in many robots. New motors that have higher torque density and careful selection of them using our optimization framework can lead to lower gear ratios and better performance.

2.4 Optimization of Actuation

There are several trade-offs and constraints in the system that make the best selection of motors and transmissions for providing efficient, agile, and fast locomotion a non-trivial task. For this purpose, an optimization framework was developed by our research group for obtaining the optimal motor and gear ratio[32]. When designing actuators, regardless of impedance, it is important to find an optimal point for energy efficiency, stability, and agility. Three optimization objectives (metrics) were proposed to provide a framework for optimizing the actuation of the system[32].

1.) Minimize the system energy consumption

2.) Minimize the passive impedance

3.) Minimize the stepping times

Our first metric is applied in the design of many robots, and by which we aim to lower the TCOT and create an energy-efficient robot. The second two metrics proposed can be used for any legged system but have been created by our research group and used for the first time to develop Mithra. As explained, a higher passive impedance creates a system that is harder to control and, also makes the system more prone to be damaged by impacts. Minimizing stepping time is not a new idea but has not previously been used as a leg-design optimization objective. Wisse et al. explain that a robot will never fall if the swing leg is able to go in front of the robot fast enough. This means that creating a robot that can step quickly is highly important for maintain balance in the face of perturbations [33]. There are several trade-offs and constraints in the system that make the best

selection of motors and transmissions for providing efficient, agile, and fast locomotion a non-trivial task. For this purpose, an optimization framework was developed by our research group for obtaining the optimal motor and gear ratio[32]. By optimizing for these factors, a Pareto front is formed, and actuators can be effectively selected and designed[32].

2.5 Summary

To summarize, Mithra was designed to create humanlike movement as accurately as possible while taking steps to ensure ease of control and energy efficiency. By developing a system that closely mimics the kinematics and weight proportions of a human, Mithra is able to achieve its motion goals. This is further aided by high-torque low-impedance actuators at every joint to allow for energy-efficient control, low passive impedance, and quiet operation. Using these strategies, Mithra can, in theory, run at 3 m/s, and while control design is not a subject of this thesis, it will provide a capable mechanical testing platform for controls research.

Chapter Three: Mechanical Requirements, Design, and Analysis

3.1 Mechanical Requirements and Design

Mithra is aimed to be capable of performing human leg motions, and because of this, there were specific movement-based goals that guided the development. It was required for each joint to have enough torque and rotational speed to match a human running at 3 m/s. In order to deliver a robust and lightweight mechanical platform, differing safety factors were set for each section. The ankle joints were required to withstand the max force load from a human running at 3 m/s with a safety factor of at least 2.5. The knee was required to have a safety factor of at least 2 for each part. A higher safety factor was important for the development of a durable ankle joint because the impacts are higher farther down the leg. Human movement data was taken from the HuMod Database, which was used to generate load and joint torques[34]. The flexion torques for the speed of 3 m/s have been shown in Figure 18.

This chapter will cover the overall actuator design, starting with a high-level layout and material choices then moving into the specifics—justification and explanation of the chosen gearbox system and specific design details of the universal joints and

linkages. Following the design summary, finite element analyses and fatigue life results will be discussed as well as the inverse kinematics of the ankle mechanism.

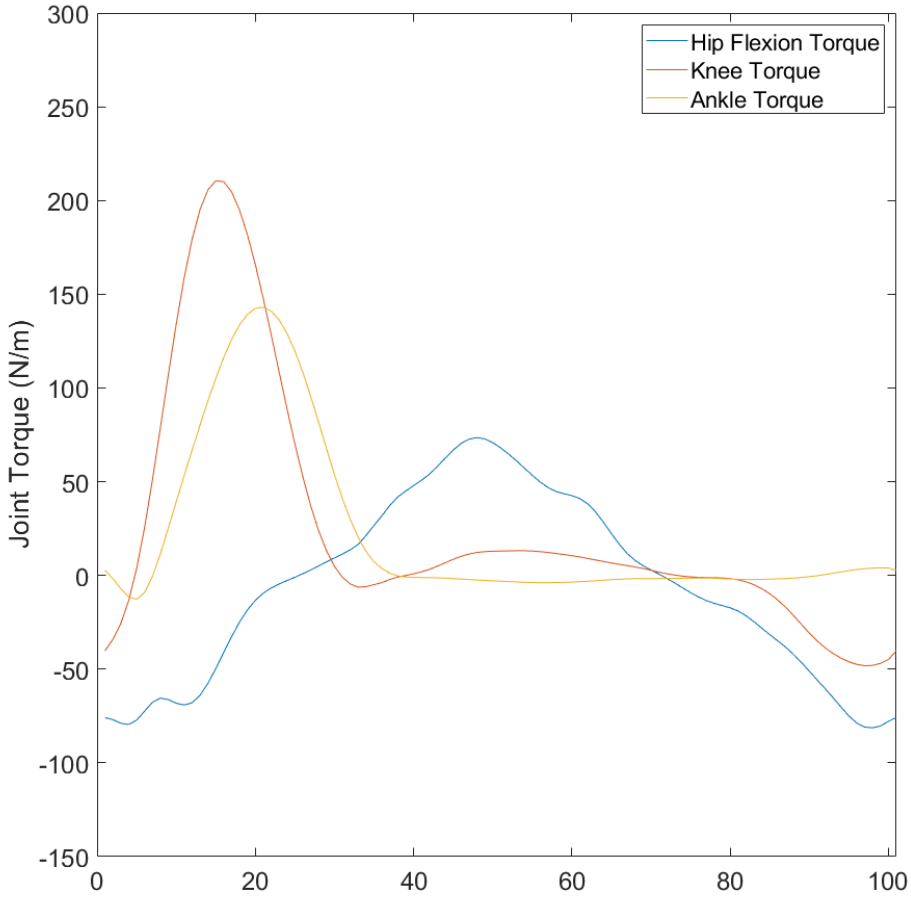

Figure 18: Flexion Torques for hip, knee, and ankle

3.1.1 Actuator Layouts

There are two main layouts for actuators depending on the gearbox and motor choices; each has its own intricacies that will be discussed later in this chapter. The goal of this section is to give an overview of the layouts.

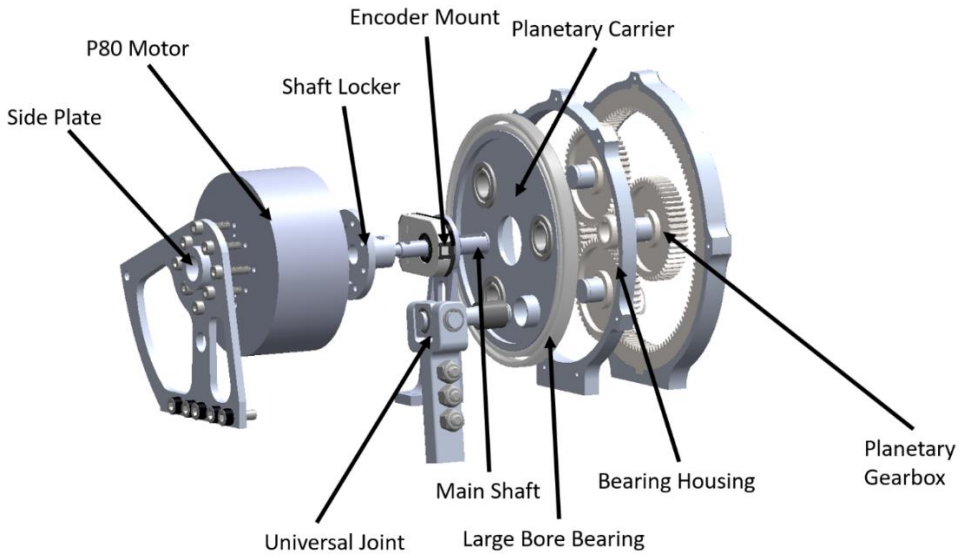

Figure 19: Ankle actuator exploded view

The ankle actuation system is shown in Figure 19. Each ankle joint is powered by two identical actuators that are placed together with a 2 mm clearance gap between them. The ankle presented specific challenges in connecting the shaft to the motor as the motor selected (T-motor P80III) was originally intended for drone propellers. The main shaft threads into the motor, and then the shaft locker allows for a small set screw to be threaded into the shaft, making the system lock together. The shaft extends into the planetary gearbox, where the output is a planetary carrier. This carrier is supported by a

thin section crossed roller bearing, which in turn is pressed into the housing. For this design, it was necessary to choose a non-disk encoder as the shaft is not fully fixed when the encoder must be installed. Moving the main shaft while a disk encoder is attached results in damage to the disk but using diskless encoders, the shaft is fixed and causes no damage during the installation process.

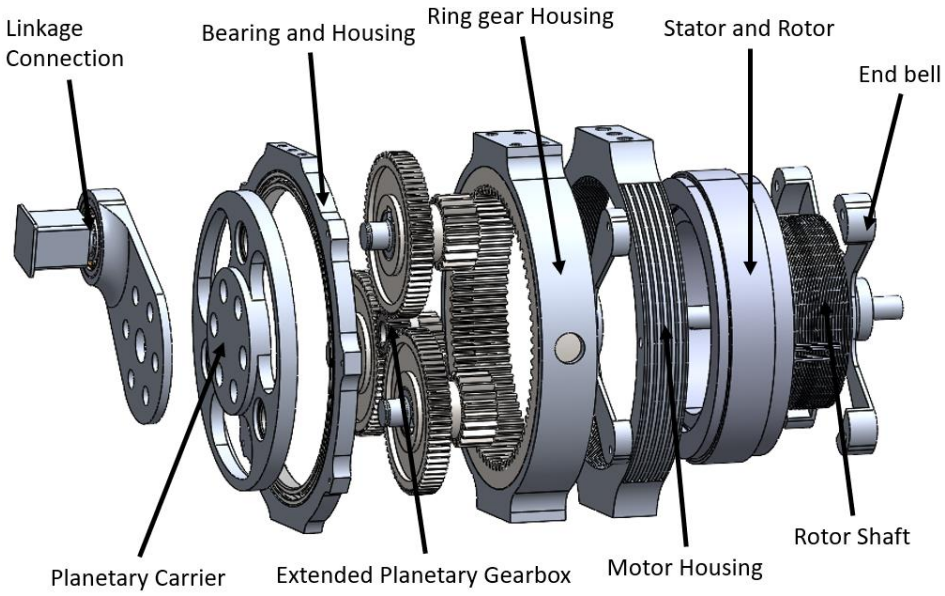

Figure 20: Knee actuator exploded view

The knee actuator features a different design than the ankle because it does not need to make use of a parallel mechanism. For the ankle actuator, there was no feasible combination of motor and gearbox that could satisfy the flexion torque and speed requirements. The best solution was to allow the motors to work together in parallel. This allowed the torque and speed requirements to be met. The knee actuator was able to meet its torque requirements with a larger gearbox and frameless motor. This actuator design features a custom motor housing and shaft design, as well as a lightweight but durable planetary carrier and linkage system.

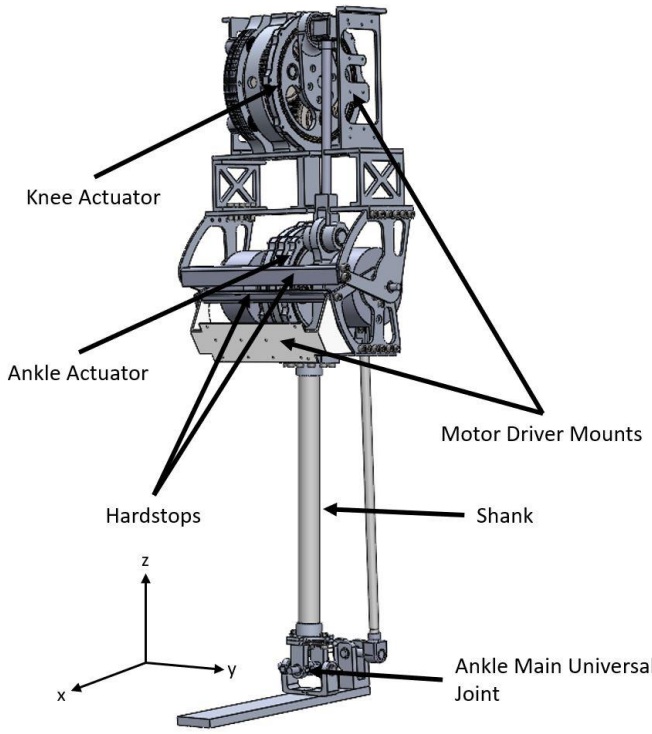

Figure 21: Full foot to knee actuator design of Mithra

The entire structure of Mithra's ankle and knee sections is shown in Figure 21. This picture includes several key pieces that are not necessarily part of the actuators but are vital for the robot to function. Two motor drivers (Odrive, Oakland, CA) mounts are both located near their respective actuators. Another key piece for Mithra is the knee joint hard stops. All hard stops contain a valley within two thin edges that allow for a piece of D3o to be placed in them. D3o is a special material commonly used in athletes' helmets to stop concussions, and it works extremely well for stopping impacts quickly and absorbing their shock.

3.1.3 Material Choices

Many materials were examined to develop an ideal strength to weight ratio for the leg, but in the end, the only feasible option for most of the structure was Al7075-T6. While Titanium is much less dense than steel and stronger than aluminum, it is far too costly to manufacture for the purposes of this prototype and heavier than desired. Al7075-T6 provides the best combination of yield strength and weight, allowing for all parts to be designed with proper safety factors and human weight proportions. The main downside of Al7075-T6 is its modulus of elasticity. With a modulus of 71.7 GPa, it is slightly more than half as stiff as Titanium Grade five and a third as stiff as steel. While overall rigidity can be important in a robot, this was developed through analyzing the parts for deflection in critical areas.

Table 2: Material properties of potential materials [35][36][37][38]

Material	Yield Strength (MPa)	Modulus of Elasticity (GPa)	Density (g/cc)
Al6061	276	68.9	2.7
Al7075-T6	505	71.7	2.81
Ti Grade 5	830	114	4.43
AISI 4140	685	205	7.85

For the shank, a carbon fiber tube was used to ensure structural strength and minimize weight; no other material can come close to the strength to weight ratio and price provided by a carbon fiber (CF) tube. While the shank CF tube is made of overlapping layers at 0-45-90-45-0 degrees, the linkages are made of pultruded carbon fiber. The main difference is the direction in which they have strength. Because of the overlapping layers, the Shank is strong to bending and axial forces. The pultruded rods

are made up of thousands of fibers, all in the same direction, with an epoxy layer holding them together. This gives the pultruded rod high axial strength and rigidity but comes at the downside of being overall weaker and less rigid to bending. They are ideal for linkages as they provide high axial strength with a smaller outer diameter than CF tubes.

3.1.4 Motor Comparisons and Selections

The P80III motor was used for the ankle actuator, providing a pre-designed housing with a maximum output torque of 9.52 Nm and a no-load velocity of 4373 RPM. The two ankle motors will work together for plantarflexion/dorsiflexion to output a large torque at high speeds allowing for a versatile ankle joint. The motor data examined for the ankle and knee motors is presented in Table 3.

Table 3: Ankle and knee motor specifications

	Allied Motion MF0127020 Custom Winding	T-Motor P80 III KV120
Motor inertia	0.00066	0.00077
Damping	0.00045	0.0008
Wire resistance	0.11	0.041
Km - motor constant (Nm/sqrt(W)	0.49	0.39
Kt - torque constant (Nm/A)	0.24	0.08
Dt or Peak torque	25.8	9.52
Maximum current	160	160
Continuous torque (Tc)	3.8	5.6
Weight (g)	1150	649
Rotor Diameter (mm)	84	91.6
Rotor Length (mm)	24.6	40
No load speed (rad/s)	294	458
Peak Current (A)	163	119
Rated Current (A)	23.75	70

For the knee, the Allied Motion MF0127020 with a customized winding was chosen to provide a high peak torque of 25.8 Nm and a no-load speed of 2800 RPM. This high torque motor allows for a knee capable of fully squatting and supporting a full

running gait. This motor, unlike the ankle motor, required a custom housing and rotor shaft to be designed. This will be investigated later in this chapter.

3.1.5 Motor Housing Design

In order to design a lightweight and compact actuator for the knee and hip setups, it was imperative that frameless motors were chosen. This allowed each motor to have a custom frame, end bells, and rotor designed specifically for the needs of each joint. The final design for the knee motor housing is displayed in Figure 22. Designing custom housing comes with its own difficulties, particularly in manufacturing, but even more advantages when it comes to design. The difficulties included designing custom end bells that would allow the stator and rotor to have a symmetrical air gap between them. The desired air gap was 0.5 mm, and this meant that the tolerance for several parts needed to be very tight. The end bells needed to be within 0.05 mm of concentricity with each other because otherwise, multiple errors could occur. The first major error that could occur was radial misalignment, meaning that the rotor is not concentric and much too close to one side. The second error that could occur was angular misalignment, which means that the rotor would be at a slight angle. These misalignment errors can cause severe motor damage, unwanted vibration, or shaft failure.

When assembling the motors, it was also important that one end bell be securely fastened to the outer housing to ensure the motor was sat with no radial misalignment. While the frameless motor presented obstacles, it also allowed for a lightweight and space-efficient housing and rotor to be designed. All frameless motor housings and rotors

were designed with AL 7075, allowing for a knee housing weight of only 270 g and a rotor shaft weight of 151 g. The rotor shaft moment of inertia, which is critical for retaining the no-load speed of the motor, was 0.00011270 kg•m^2.

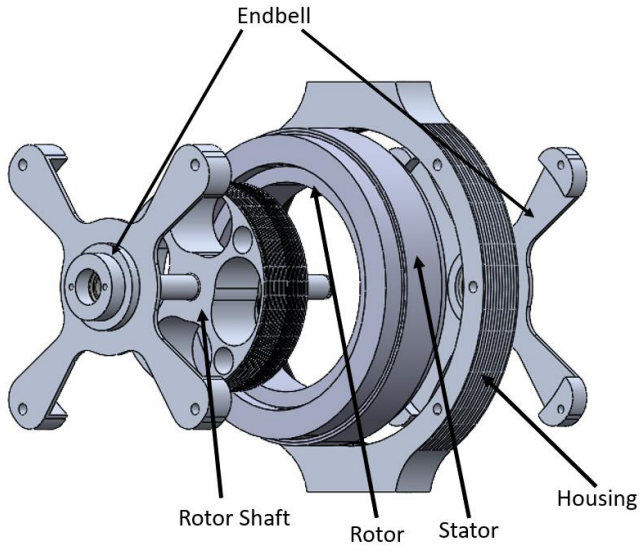

Figure 22: Motor housing design

There are several other advantages that come along with a custom housing design. Heat fins were designed along the outside of the housing that can improve the heat transfer for the motor. Another addition was custom encoder mounts added onto the outer end bell. This was important because it allows for easy and safe encoder placement. The versatility this motor provided made it possible to build a gearbox into the middle of the thigh that fits into a 142 ×164×174 mm package.

3.2 Gearbox Design

Modern robots use a variety of transmission methods, all with certain strengths and weaknesses. The most popular among these methods are harmonic drives, ball screws, and cycloid drives. Harmonic drives and cycloid drives both allow for high gear

ratios, but the harmonic drives lack efficiency, and the cycloid drives are subject to backlash, gear ratio rippling, and require high manufacturing precision. Ball screws are also able to reach high gear ratios while being robust and efficient. While they all have their advantages, the high impedance and lower rates of efficiency than planetary gearboxes are why we decided against them. Using a variation of the planetary gearbox setup, we were able to break through the normal limitations of planetary gearbox systems.

3.2.1 Gearbox Layouts

Mithra's actuator optimization took two types of gearboxes into account, a single-stage planetary gearbox and a single-stage stepped planet compound planetary gear transmission (SPC-PGT). Planetary gear systems were the obvious choice for Mithra because of their high efficiency and low backlash. However, normal planetary gearboxes bring with them a geometric limitation on reduction ratios, 10:1 or less. While Mithra aimed to feature low-impedance actuators, a reduction ratio higher than 10 was necessary to realize humanlike motion with the legs. An SPC-PGT is an extension of the single-stage planetary that allows for higher gear ratios to be reached by introducing three extra gears into the system[30] . The SPC-PGT, as shown in Figure 23, is comprised of a sun gear, sun-planet gear, ring-planet gear, and ring gear. The sun planet rotates around the sun gear, and the sun planet is fixed onto a shaft that connects to the ring planet. The ring planets then rotate around the ring. This design adds weight, but the optimization for the knee required a gear ratio of 15:1, and this gearbox allows us to reach that ratio.

The single-stage planetary gearbox utilized for the ankle is a normal configuration, pictured in Figure 24, using the sun gear as the input with the planetary carrier as the output. The ring gear is fixed within its housing. It was important to have the planetary carrier as the output of the system as the goal of these actuators was to create a four-bar linkage. Other configurations would make developing a robust gearbox and rigid linkage system more complicated.

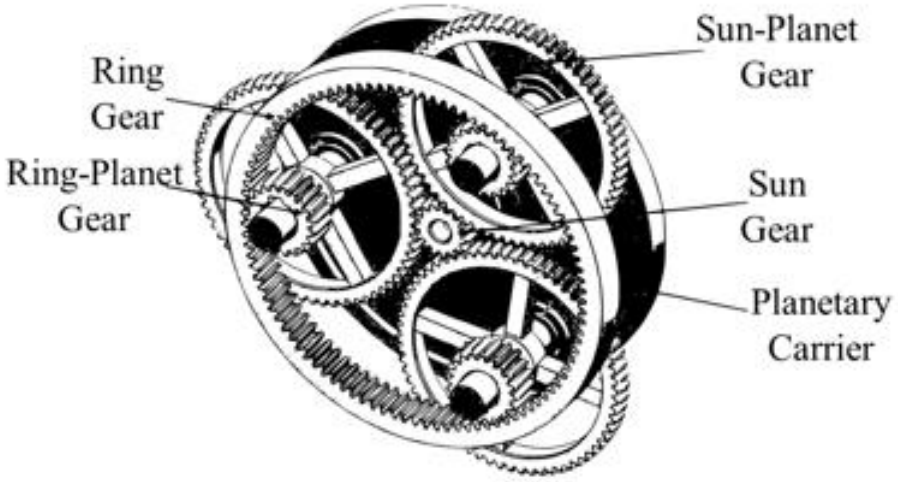

Figure 23: A schematic of SPC-PGT transmission system

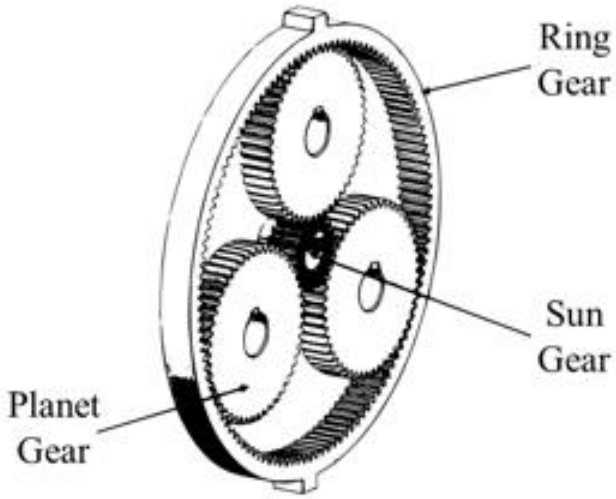

Figure 24: Planetary gearbox schematic

The equations to determine the gear ratio of a standard planetary gearbox with the sun gear as the input and planetary carrier as the output is shown in Equation 1, where $\frac{\omega_m}{\omega_j}$ is the total reduction ratio in terms of the joint and motor velocities, D_r is the diameter of the ring gear, and D_s is the diameter of the sun gear.

$$\frac{\omega_m}{\omega_j} = \frac{D_r + D_s}{D_s} \tag{1}$$

$$\frac{\omega_m}{\omega_j} = 1 + \frac{D_r D_{sp}}{D_s D_{rp}} \tag{2}$$

Equation 2 presents the gear ratio for a SPC-PGT, where the variables are the same as in Equation 1, except for the addition of D_{sp} which is the diameter of the sun-planet and D_{rp} which is the diameter of the ring planet.

3.2.2 Lewis Bending Equations

The Lewis bending equation is the standard for determining the stress in gear teeth and whether or not they can withstand their loads. Each gear was tested with these equations to make sure it could withstand maximum motor torque with a safety factor of at least 2.0.

$$\sigma_{Flim} = F_t \frac{Y_F Y_\varepsilon Y_\beta}{m_n b} \frac{K_V K_O}{K_L K_{FX}} S_F \tag{3}$$

Equation 3 presents the Lewis bending equation. The variables serve to describe machine conditions that can drastically impact performance. The variables are as follows:

F_t = Tangential Force
Y_F = Tooth Profile Factor
Y_ε = Load Distribution Factor
Y_β = Helix Angle Factor
m_n = Gear Module
b = Gear Width (mm)
K_V = Dynamic Load Factor
K_O = Overload Factor
K_L = Life Factor
K_{FX} = Root Stress Dimension Factor
S_F = Safety Factor

Several of these variables are equal to 1 in Mithra's gearboxes. The variables equal to 1, in this case, are Y_β, K_{FX}, $K_{L.}$ The helix angle factor will be one in all cases where non-helical gears are used, and the dimension root factor is almost always unity. The life factor, in this case, is one as well so that these gears will not need to be replaced and have a maximum life cycle.

On the other side, there are several factors that are particularly important in the gearbox system. K_V, $K_{O,}$ Y_ε are the variables that significantly impact the system. The dynamic load factor matters as it directly correlates to the pitch line velocity along the teeth and can be quite high because of the low ratio. The Overload factor measures the overall shock in the system, and while the electric motors drive the system smoothly, this factor is high in Mithra as the ground reaction forces create a higher impact load in the system.

Lastly, an important distinction when using the Lewis bending equation with a planetary gear system is multiplying the acceptable root stress by two-thirds as the system is bi-directional, lowering the overall stress a tooth can withstand.

Using the Lewis bending equation, it was determined that in order to design gearboxes with the required safety factor, we needed them to be from two differing materials. Some are made of SCM415 and some of S45C. SCM415 is a low carbon steel that is carburized to have a hardness of 55-60 HRC and a bending root strength of 49 kgf/mm^2[39]**.** S45C is a steel with a higher carbon content, having a lower bending strength of 28.5 kgf/mm^2 [39] and a hardness less than 194 HRB if not thermally refined. All gears were selected off the shelf from KHK, SDP SI, and KG gears in order to lower costs and save time, but modifications were made to the gears in order to lower their weights and moments of inertia.

3.2.3 Developing the Gearbox

While there are many combinations for a gearbox for any specific gear ratio, there are only a finite number of gears available, materials available, and limitations on size and weight. In order to design an optimal gearbox for each ratio, Equation 2 and Equation 4 were input into MATLAB along with all available stock gears. The MATLAB script can be found in the Appendix. Equation 4 mathematically proves if an SPC-PGT system will mesh by subtracting the diameter of each gear. If the equation results in a number greater than zero, the gears are too small to mesh together completely, and if the answer is less than one, they will be too large to mesh. These configurations were then analyzed for strength, and if they did not have at least a safety factor of two, they were eliminated.

$$D_R - D_{RP} - D_{PS} - D_S = 0 \tag{4}$$

Table 4: Single-stage planetary gearbox for the ankle actuators

Joint	Sun	Planet	Ring	Ratio
Ankle	SCM415 Module 1 20 Tooth	SCM415 Module 1 50 Tooth	S45C 120 Tooth Module 1	7

Table 5: SPC-PGT configurations of the knee and hip actuators

Joint	Sun Gear	Sun-Planet	Ring-Planet	Ring	Ratio
Knee	SCM415 Module 1 20 Tooth	SCM415 Module 1 70 Tooth	SCM415 Module 1.5 20 Tooth	S45C 80 Tooth, Module 1.5	15
Hip Abduction/Flexion	SCM415 Module 1 20 Tooth	SCM415 Module 1 20 Tooth	SCM415 Module 1.5 20 Tooth	S45C 80 Tooth, Module 1.5	15
Hip Yaw	SCM415 Module 1 20 Tooth	SCM415 Module 1 20 Tooth	SCM415 Module 1.5 20 Tooth	S45C 80 Tooth, Module 1.5	15

Finalized gearbox configurations are seen in Table 4 and Table 5. The ankle gearbox gives a reduction ratio of 7 for each gearbox, making use of SCM415 gears to provide the necessary strength. The knee and hip gearboxes are all 15:1. Even though they all have differing needs for maximum torque outputs, the multi-objective optimization found a good trade-off among the previously discussed objectives with this gear ratio. While the reduction ratio is the same for all gearboxes, there are key differences in the structure of the spur and ring gears.

While the three extended planetary gearboxes are almost identical, they contain key differences. The knee makes use of a custom ring gear as it produces the highest torque out of any joint. It was determined from the Lewis bending equations that the ring

needed to be 25 mm wide instead of the off-the-shelf 15 mm to withstand the stress. The hip abduction/flexion and yaw both are able to use off-the-shelf ring gears at a normal thickness but have a key difference in their sun gear. The yaw gearbox makes use of a gear featuring a smaller keyway as its output torque was much less than the other actuators.

3.2.4 Fixing the Ring Gears

Fixing the ring gear within its housing was a critical step to creating a working actuator. In order to fix the ring gear, a modification had to be made to the ring gear, heavy-duty set screws needed to be used, or the housing needed modification. In the end, three different methods were developed to fix each ring gear reliably and efficiently. For the ankle ring gears, space was especially important, and thus they are each 10 mm thick, which does not leave room for a set screw bigger than 5 mm. Several set screws could have been placed, but it was determined that the easiest way was to have a key cut via wire EDM into the top and bottom of the gear. The keys, along with a tight press fit into the aluminum housing, made for a rigid fix of the gear.

The knee and hip gears both presented similar challenges, and thus a similar solution was developed on each. For the 25 mm thick knee ring gear, two holes were drilled and tapped for M12 bolts on either side. A tight-fitting clearance hole was made in the housing, and bolts were screwed 6 mm deep. The hip ring gears have a thickness of only 15 mm, so smaller M6 bolts were used.

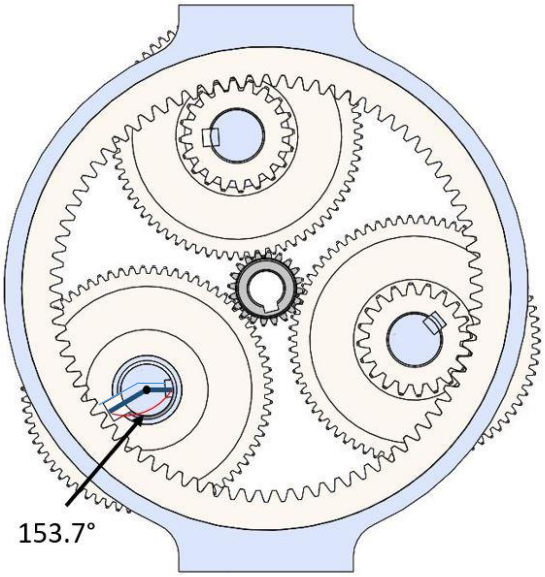

Figure 25: Knee gearbox key measurement

Fixing the ring gear was the main issue presented in the gearbox design; however, the knee and hip presented another issue. Because of the SPC-PGT setup, any gear system should fit within the ring gear, but to make this work, the keyed slots needed to be an exact angular distance apart. The gear system was modeled in SolidWorks with accurate gear mates, and measurements of where the keys should be were taken directly from the modeled assembly and resulted in an angular distance of 153.7 degrees(Figure 24).

3.2.5 Planetary Carrier Design

The ankle was designed with two single-stage planetary gearboxes; however, because of the size of the gears and the placement of our linkage, it was necessary to have an offset three-planet gearbox so that each planet gear would be able to mate with the ring gear. In order to determine the placement of the gears so that the sun gears meshed with the ring gear, a script was developed to iterate through all angles in MATLAB and validate them with Equation 5.

$$\frac{(Z_a+Z_c)\theta}{180} = \text{Integer} \tag{5}$$

In Equation 5, Z_a is the number of teeth on the sun gear, Z_C is the number of teeth on the ring gear, and θ is half the angular distance between planets. It was found that the angles of 108 and 126 allowed for all criteria to be met. This means that the separation between two sets of planets was 126 degrees and the other was 108 degrees separated. In this case, if each planet was 120 degrees apart, the formula would equal 113.33, and because this is not an integer, the gears would not mesh.

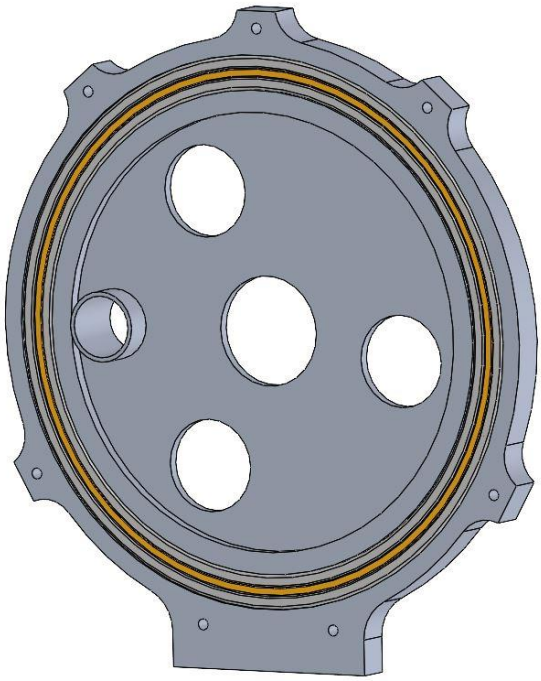

Figure 26: Ankle planetary carrier

After calculating the angles for the gears, the rest of the planetary carrier was simple to design. The final design is pictured in Figure 26. The outer diameter and thickness were both dictated by the size of the thin section bearings chosen, meaning the most difficult part was selecting tolerances from the bearing's technical sheets. While there are several differences in the planetary carriers between the ankle, knee, and hip joints, there is only one main difference. This main difference is that the ankle and knee joints both used higher diameter bearings to encase the carrier, but for the hip, it was found to be cheaper and easier to use lower diameter bearings that the carrier could attach on the outside of.

3.3 Mechanism Design

3.3.1 Ankle Linkage Design

The ankle linkage utilizes a single-stage planetary gearbox, and this means that it cannot achieve a gear ratio above 7:1, which did not allow for enough torque output from the actuator. In order to reach the required torques, it was necessary to design a linkage with a reduction ratio of 1.6, Figure 27 shows such a linkage in 2D. The ankle's ability to move in two degrees of freedom is generated by two independently driven actuators. To enable this motion, each connection from the ankle to the foot must also have 2 DOF. The best way to achieve this is through the design of custom universal joints. The design for each custom joint will be detailed later in this chapter.

Because each connection from the gearbox to the foot is a 2 DOF universal joint, the foot can achieve plantarflexion/dorsiflexion movement by rotating the planetary carriers in the same direction at the same speed. Inversion/eversion is created by the two planetary carriers moving opposite each other or at different speeds. The linkages are able to work together and create twice the torque for their movements while retaining motor speed. This allows for a high torque ankle that can move at high rotational speeds. The lengths of the ankle linkage can be seen below in Figure 27, and the 3D extension of the mechanism in Figure 28

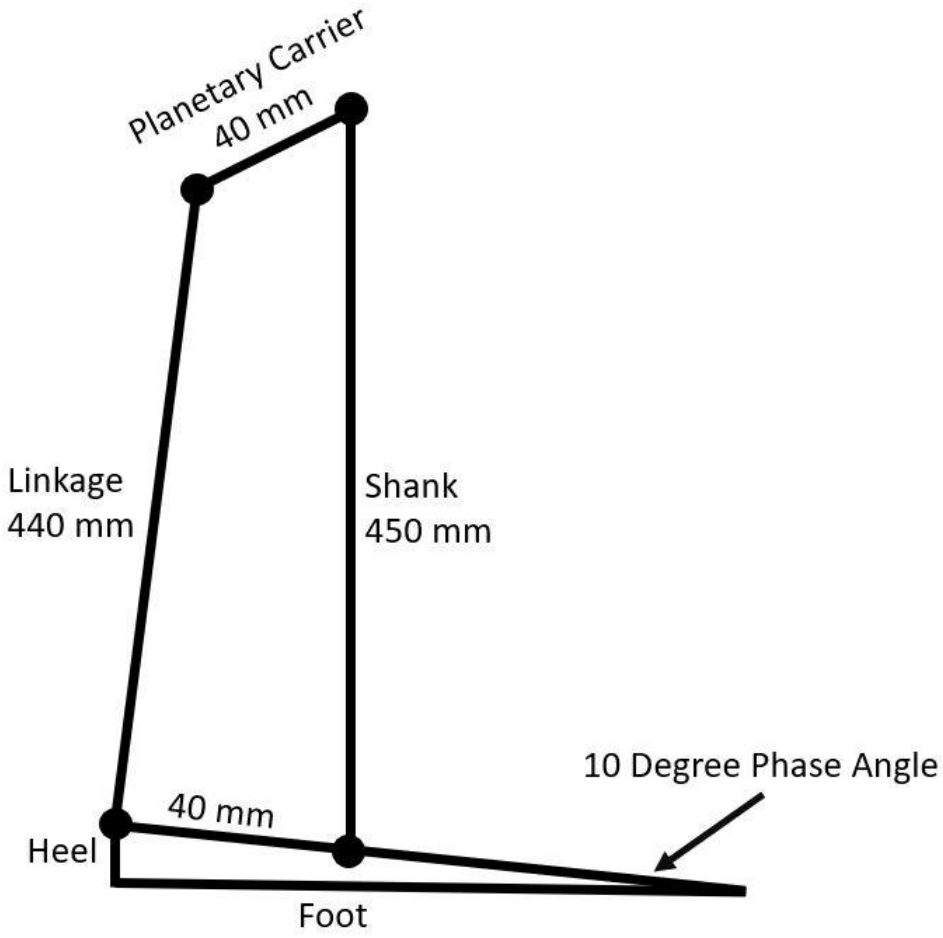

Figure 27: Ankle mechanism in 2D

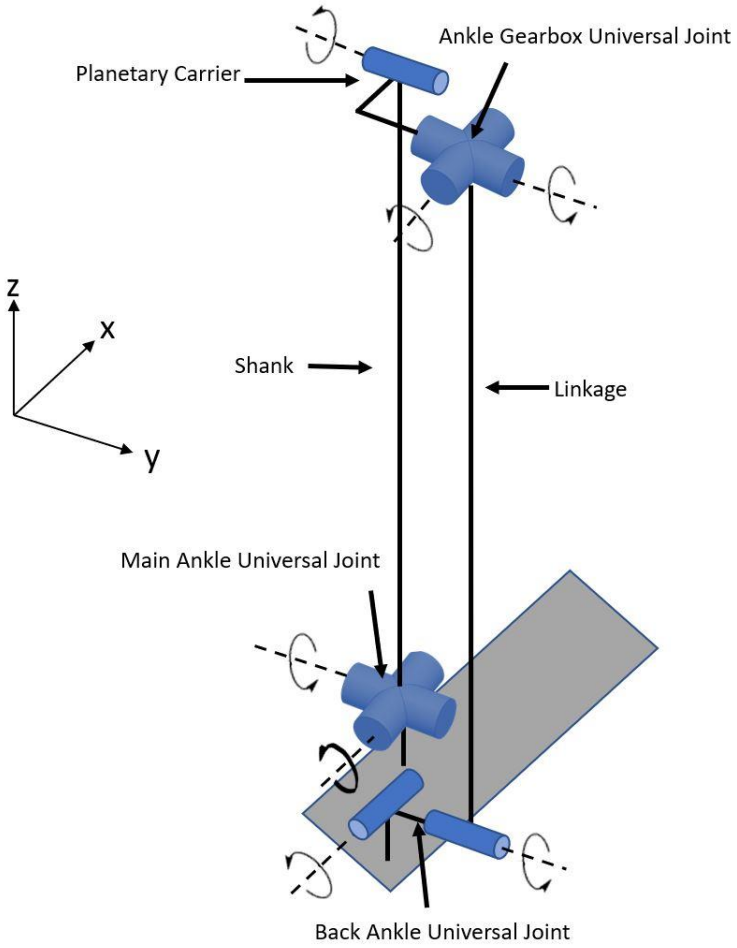

Figure 28: Ankle 3D mechanism representation

3.3.2 Knee Linkage Design

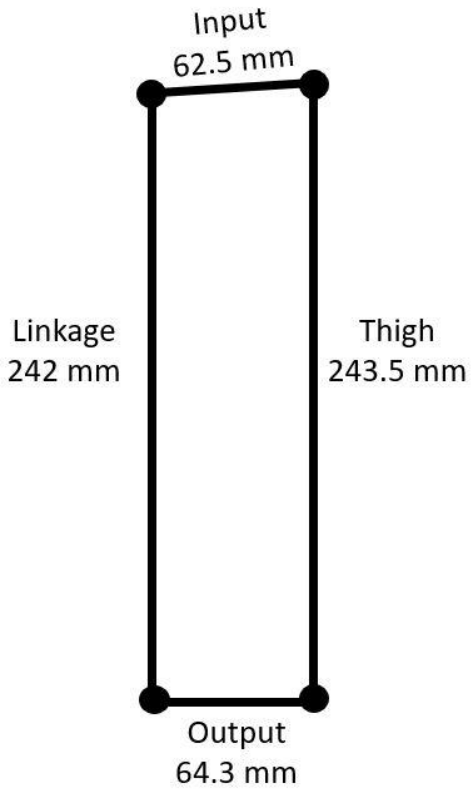

Figure 29: Knee Four-bar linkage diagram

While the knee is only 1 DOF, it also uses a linkage, but for distal mass reduction. A 10.97 mm diameter pultruded carbon fiber rod attached to a planetary carrier and a fixed end at the knee joint, this rod is shorter and weighs only 26.87 g. The input link is 62.5, the output link is 64.3 mm, and the two long links are 243.5 mm and 242 mm. This configuration is able to create a motion that is roughly 1:1 between the input and output links. The optimization results showed that the gearbox can be used without a linkage for the knee, and thus the four-bar linkage was used merely to reduce the distal mass.

3.3.3 Universal Joint Design

The ankle joint needed to have a 2 DOF mechanism that allowed for full human plantar/dorsiflexion and inversion/eversion. This means that several unique universal joints were needed to fit the strength, weight, and motion requirements of the leg. Three were designed in total, one for the Shank to foot connection, one to connect the back of the ankle to the linkage, and the last to connect the linkage to the planetary carrier.

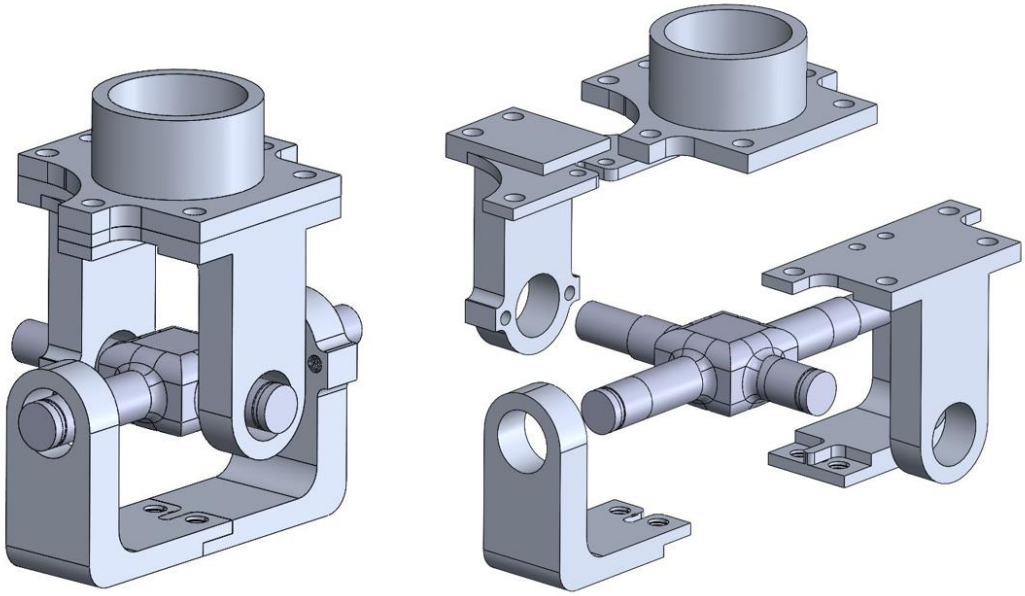

Figure 30: Main Ankle Universal Joint

The Main Ankle Universal Joint needed to handle high leg forces while simultaneously allowing for two absolute encoders to be mounted on it for joint position feedback. One on the plantarflexion/dorsiflexion plane and one on the inversion/eversion plane. This meant it was necessary to have a wide base aligned with the flexion axis of the ankle (left to right) so that the encoders and their wires would not interfere with the desired range of motion. What makes this joint unique is the way it can be manufactured. The left and right sides of the yoke have a key and key slot, respectively, so that they can

slip together. A fully assembled and exploded view of the universal joint is pictured in Figure 30.

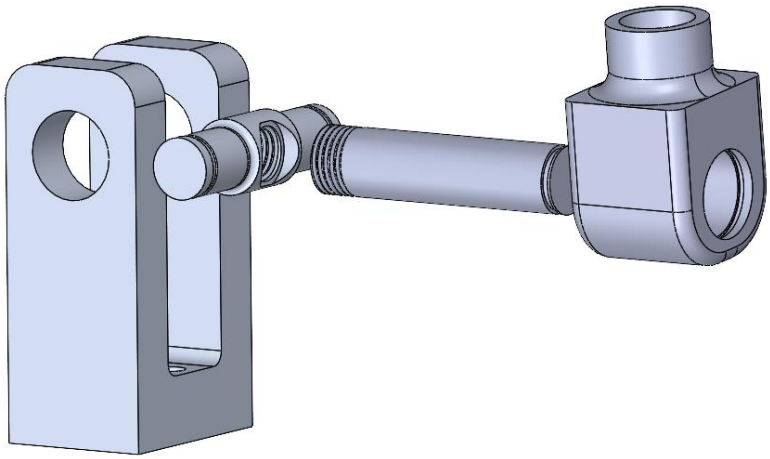

Figure 31: Back Ankle Universal Joint exploded view

The Back Ankle Universal Joint is pictured in Figure 31. The joint load was less critical on the Back Ankle Joint because it was split between two joints, but it was necessary for it to extend off the foot. The extension creates asymmetry in the joint, meaning the axes of rotation are only intersecting in one plane. Usually, a universal joint will feature a cross-shaped piece with the yokes directly above each other. The asymmetry was necessary because of the layout of the gearbox above; with both gearboxes being in the middle, the linkages needed to connect at a point wider than the foot. A universal joint designed like this was made possible by creating a shaft with one end threaded that connected to a perpendicular shaft with a large threaded hole. This meant that the shafts could slide through their bearings and then connect to the linkage; an example is pictured in Figure 32, with an arrow showing a simplified assembly.

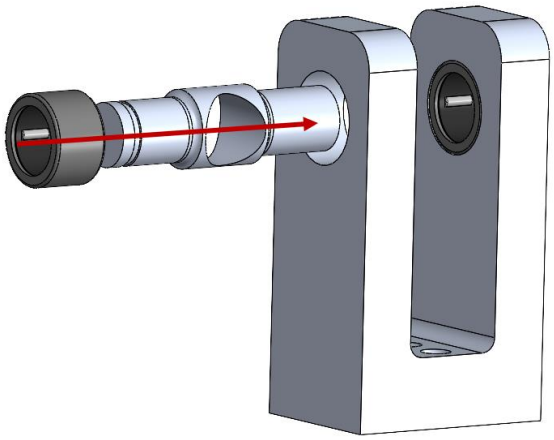

Figure 32: Back Ankle Universal Joint simplified build

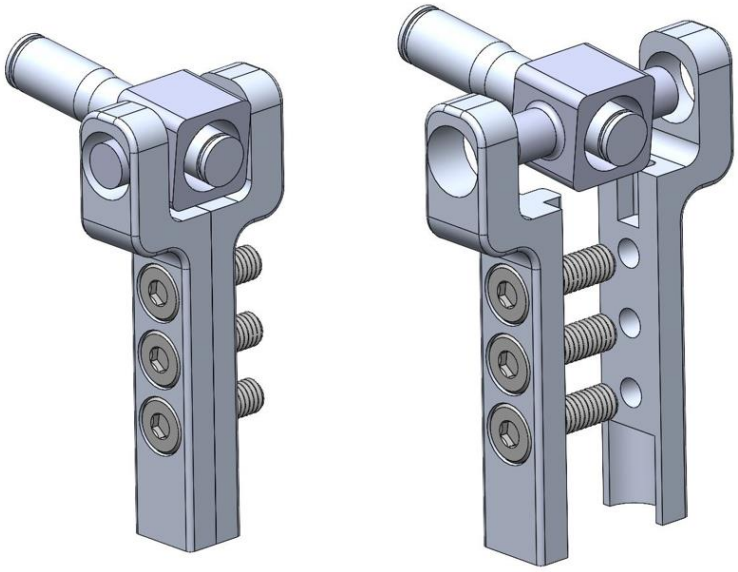

Figure 33: Ankle Gearbox Universal Joint

The main goal for the Ankle Gearbox Universal Joint was size. In earlier versions of the design, a super swivel ball end rod was used that had a 55-degree range, but it proved to have high friction. The replacement needed to take up as little space as possible to not impact the range of the ankle. This was accomplished by using small needle roller bearings that can fit on the pre-designed shaft and a two-sided asymmetrical yoke that

slips together with keys and is then bolted. Ultra-low head height bolts were utilized so they would sit flat with the surface, pictured in Figure 33

3.3.4 Bearing Selection

Several types of bearings were necessary to facilitate differing conditions. For the universal joints and high load-bearing joints, differing sizes of needle roller bearings were used. These bearings allow for high loads to be tolerated, although this comes at the price of rotational speed. Five varied sizes of needle roller bearings were selected for Mithra's knees and feet. Large cylindrical roller bearings were necessary for the extremely high torque requirements of the knee, and flanged ball bearings were chosen for the planetary carriers as they offer smooth rolling and do not need to handle large loads. For the outside of the planetary carrier's thin section, roller bearings were originally picked as they would provide a smooth and stable platform for the carriers to be mounted into, but due to stock shortages, crossed roller bearings were used. These bearings have much higher load-bearing capabilities, but this comes at the price of rotational damping.

3.4 Inverse Kinematics of Mithra's Ankle

Developing a closed-form inverse kinematics solution is a difficult and necessary step of robotic mechanism design for several reasons. Without being able to accurately know where the foot should be, the controls would have no way of being accurate. The second reason is for force analysis. In any robot, knowing the exact position of each part

when certain forces are applied can be vital to creating a proper model for analysis. In the case of Mithra, it is especially important because the back linkage rods are pultruded carbon fiber. This means that they are strong to axial forces but weaker to bending forces. With a complete inverse kinematics model, we can find the maximum forces not only in the anteroposterior direction and vertical direction but also in the mediolateral direction.

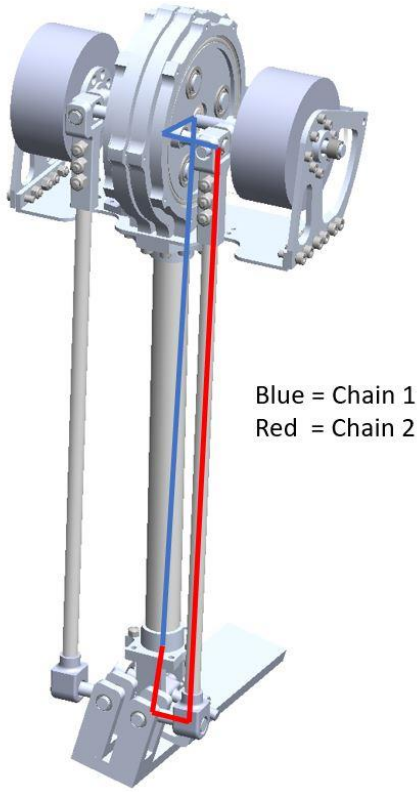

Figure 34: Outline of the kinematic chains

The ankle was designed as two symmetric kinematic loops at the sides of each leg. While the forward kinematics of the parallel mechanism (here: when we have the motors' motions and want to determine foot flexion and inversion/eversion angles) is in general not solvable, the inverse kinematics is usually more straightforward. We do this by creating a loop, as in Figure 34, by going from the ankle to the center of the top

universal joint from two different paths (shown by red and blue). The variables for the first chain are detailed in Figure 35.

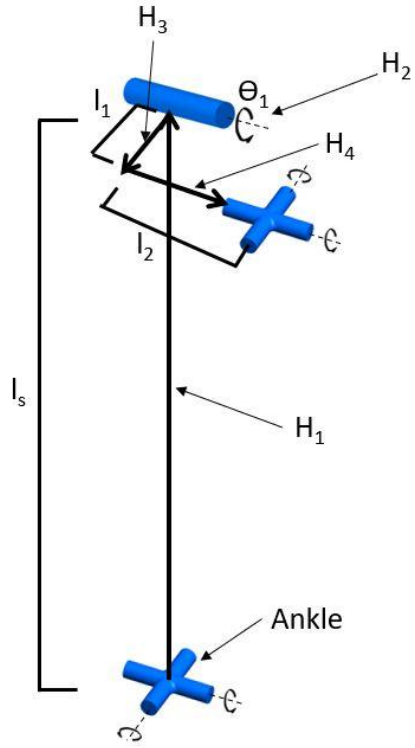

Figure 35: Kinematic chain one with variables

The first chain starts with a homogenous transformation directly up the shank to the middle of the planetary carrier, labeled as H_1[40]. Our first joint variable is called θ_1 (Figure 35), and the second homogenous transformation, H_2, represents the rotation due to this angular motion:

$$H_1 = \begin{bmatrix} 1 & 0 & 0 & 0 \\ 0 & 1 & 0 & 0 \\ 0 & 0 & 1 & l_s \\ 0 & 0 & 0 & 1 \end{bmatrix} \tag{6}$$

$$H_2 = \begin{bmatrix} \cos\theta_1 & 0 & -\sin\theta_1 & 0 \\ 0 & 1 & 0 & 0 \\ \sin\theta_1 & 0 & \cos\theta_1 & 0 \\ 0 & 0 & 0 & 1 \end{bmatrix} \tag{7}$$

The chain then consists of a translation from the center of the planetary carrier in the anteroposterior and then another translation in the positive or negative mediolateral direction (depending on which kinematic chain on which side of the leg the formulation is written for) to reach the universal joint, these transformations are characterized by H_3 and H_4 ,respectively. This is the point where the two kinematic chains connect and create a loop.

$$H_3 = \begin{bmatrix} 1 & 0 & 0 & -l_1 \\ 0 & 1 & 0 & 0 \\ 0 & 0 & 1 & 0 \\ 0 & 0 & 0 & 1 \end{bmatrix} \tag{8}$$

$$H_4 = \begin{bmatrix} 1 & 0 & 0 & 0 \\ 0 & 1 & 0 & -l_2 \\ 0 & 0 & 1 & 0 \\ 0 & 0 & 0 & 1 \end{bmatrix} \tag{9}$$

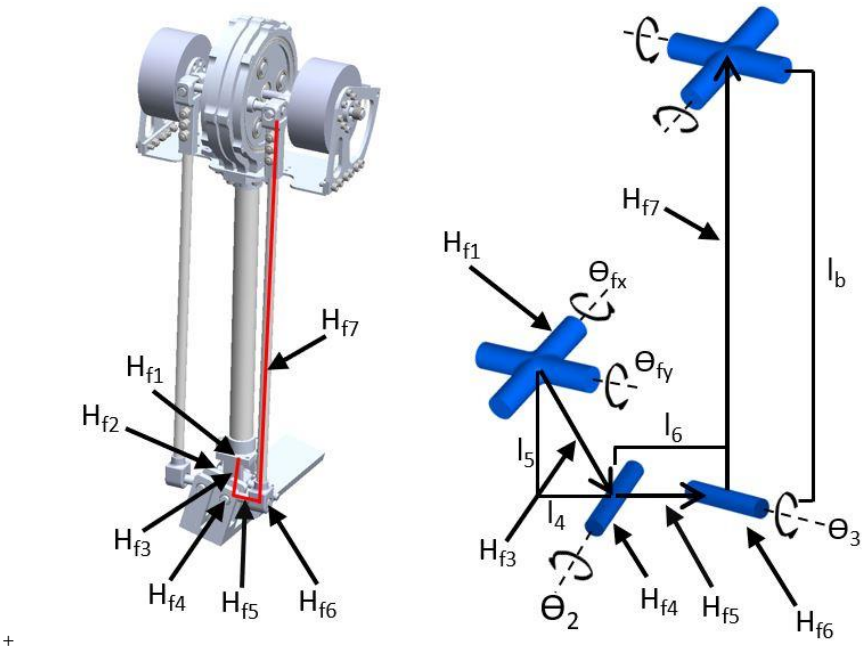

Figure 36: Kinematic chain two with corresponding variables and homogenous transformations

In order to develop the second kinematic chain, which is presented in Figure 36, the input angles of the foot must be considered. The foot angles are denoted as θ_{fx} and θ_{fy}, where θ_{fx} is the inversion/eversion angle and θ_{fy} is the plantarflexion/dorsiflexion angle. These two angles are both known from the considered running gait cycle, and this allows to find the homogenous transformation H_{f1} and H_{f2} corresponding to these two rotations:

$$H_{f1} = \begin{bmatrix} 1 & 0 & 0 & 0 \\ 0 & \cos\theta_{fx} & -\sin\theta_{fx} & 0 \\ 0 & \sin\theta_{fx} & \cos\theta_{fx} & 0 \\ 0 & 0 & 0 & 1 \end{bmatrix} \tag{10}$$

$$H_{f2} = \begin{bmatrix} \cos\theta_{fy} & 0 & -\sin\theta_{fy} & 0 \\ 0 & 1 & 0 & 0 \\ \sin\theta_{fy} & 0 & \cos\theta_{fy} & 0 \\ 0 & 0 & 0 & 1 \end{bmatrix} \quad (11)$$

Next, a translational homogeneous transformation can be found from the center of the Ankle joint to the center of the inside pin joint at the heel. This is represented by H_{f3}:

$$H_{f3} = \begin{bmatrix} 1 & 0 & 0 & -l_4 \\ 0 & 1 & 0 & -l_5 \\ 0 & 0 & 1 & z_f \\ 0 & 0 & 0 & 1 \end{bmatrix} \quad (12)$$

The angle of this pin joint represents the second joint angle in the kinematic chain that we want to solve for. It is represented by θ_2 and the homogeneous transformation embodying the corresponding rotation is shown by H_{f4}:

$$H_{f4} = \begin{bmatrix} 1 & 0 & 0 & 0 \\ 0 & \cos\theta_2 & -\sin\theta_2 & 0 \\ 0 & \sin\theta_2 & \cos\theta_2 & 0 \\ 0 & 0 & 0 & 1 \end{bmatrix} \quad (13)$$

Between the two pin joints at each side of the heel, there is an offset, which is represented by a translational homogeneous transformation H_{f5}:

$$H_{f5} = \begin{bmatrix} 1 & 0 & 0 & 0 \\ 0 & 1 & 0 & -l_6 \\ 0 & 0 & 1 & 0 \\ 0 & 0 & 0 & 1 \end{bmatrix} \quad (14)$$

Next, the rotation around the outside pin joint of the heel is embodied by a rotational homogeneous transformation, H_{f6}:

$$H_{f6} = \begin{bmatrix} \cos\theta_3 & 0 & -\sin\theta_3 & 0 \\ 0 & 1 & 0 & 0 \\ \sin\theta_3 & 0 & \cos\theta_3 & 0 \\ 0 & 0 & 0 & 1 \end{bmatrix} \tag{15}$$

wherein θ_3 denotes the rotation angle and is the third joint angle in the loop to be solved. Finally, a translational homogenous transformation along the pultruded rod, H_{f7}, brings us back to the center of the top universal joint:

$$H_{f7} = \begin{bmatrix} 1 & 0 & 0 & 0 \\ 0 & 1 & 0 & 0 \\ 0 & 0 & 1 & l_b \\ 0 & 0 & 0 & 1 \end{bmatrix} \tag{16}$$

Now that we have formulated these homogenous transformations, we are able to use three properties of the system to solve for our three unknown joint variables, i.e., θ_1, θ_2, and θ_3. The first property is that the two links extending from the Back Universal Joint up the linkage are always perpendicular to each other, and because these links are of fixed lengths, the Pythagorean theorem can be used to find the length of the hypotenuse. This length is fixed, and the angles θ_2 and θ_3 are irrelevant to this calculation. Now that the total distance from the inner heel pin to the center of the top universal joint is known, having the foot angles, we can solve for θ_1. For this purpose, we write:

$$\|d_1 - d_2\| = \sqrt{{l_b}^2 + {l_6}^2} \tag{17}$$

where $d_1$is the location of the center of the top universal joint and $d_2$is the inner heel pin center point, both w.r.t the ankle. These vectors can be seen in Figure 37.

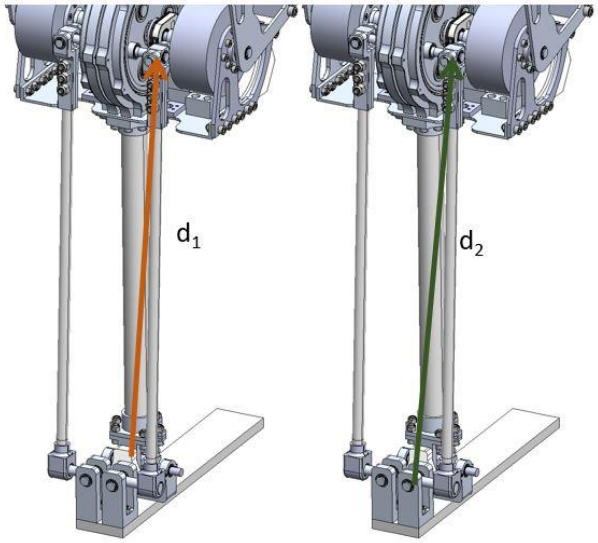

Figure 37: Position vectors for the top universal joint, d_1, and the inner heel joint d_2.

While the position of d_2 is known from the foot angles, θ_{fx} and θ_{fy}, the position of $d_1$is dependent on θ_1, represented as follows:

$$d_1 = \begin{bmatrix} -l_1 \cos\theta_1 \\ -l_2 \\ l_s - l_1 \sin\theta_1 \end{bmatrix} \tag{18}$$

After expanding out Equation 17 and simplifying, we reach the following equation:

$$\sin\theta_1 + a\cos\theta_1 = b \tag{19}$$

Where a and b depend only on the parameters of the system and foot angles, and not θ_1.

Equation 19 can be solved to obtain:

$$\sin\theta_1 = \frac{2b \pm \sqrt{4b^2 - 4(b^2 - a^2)(1 + a^2)}}{2(1 + a^2)} \tag{20}$$

$$\theta_1 = \sin^{-1}\left(\frac{b \pm a\sqrt{(1+a^2)-b^2}}{1+a^2}\right) \tag{21}$$

where plus and minus corresponds to the left and right loops, respectively.

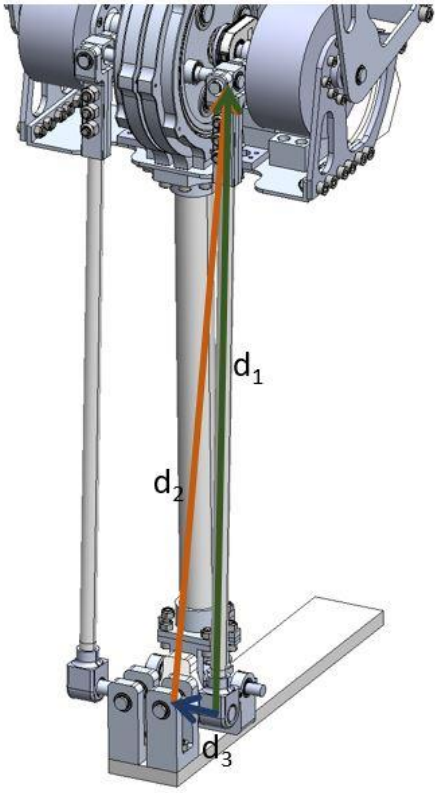

Figure 38: The associated vectors with the position of the outer heel joint with respect to the top universal joint are always perpendicular to each other.

The perpendicularity of the above two links offers another property in that the dot product of the corresponding vectors should always be zero. The vectors referenced can be seen in Figure 38, and we use the following equations to solve for θ_2:

$$(d_3 - d_1) \cdot (d_3 - d_2) = 0 \tag{22}$$

$$a_2 \sin\theta_2 + b_2 \cos\theta_2 + l_6 = 0 \tag{23}$$

where, like before, a_2 and b_2 are independent of θ_2. We can solve this equation to obtain:

$$\sin\theta_2 = \frac{-a^2 l_6 \sqrt{{l_6}^2 a^2 - (a^2 + b^2)({l_6}^2 - b^2)}}{a^2 + b^2} \tag{24}$$

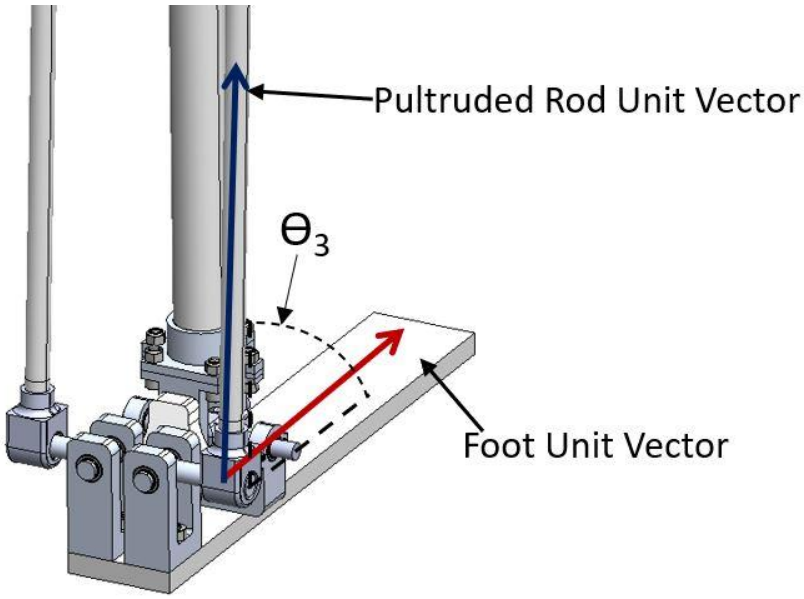

Figure 39: Ankle unit vectors

To find θ_3, we note that it is the angle between the unit vectors in the direction of the pultruded rod and the local x axis attached to the foot, pictured in Figure 39. The latter unit vector can be found by the rotation matrix of the foot angles:

$$\text{Foot Unit Vector} = H_{f1} H_{f2} \begin{bmatrix} 1 \\ 0 \\ 0 \end{bmatrix} \tag{25}$$

The unit vector in the pultruded rod direction can be found by subtracting the position of the top universal joint (its top-end) from the position of the outer heel joint (its bottom end). The top-end can be found from the first kinematic chain above, and the bottom end can be obtained from the second chain. Note that for the top end, we only need θ_1 and for the bottom end, we only need θ_2, and both of them have been calculated in the above. We have:

$$\text{Top end position} = \ d_1 = \begin{bmatrix} -l_1 \cos\theta_1 \\ -l_2 \\ l_s - \ l_1 \sin\theta_1 \end{bmatrix} \tag{26}$$

$$\text{Bottom end position} = \ d_3 \ = H_{f1}H_{f2}H_{f3}H_{f4}H_{f5}\begin{bmatrix} 0 \\ 0 \\ 1 \end{bmatrix} \tag{27}$$

$$\text{Pultruded Rod unit vector} \ = \frac{d_1 - d_3}{l_b} \tag{28}$$

$$\theta_3 = \ \cos^{-1}(\text{ Pultruded Rod unit vector} \cdot \text{Foot Unit Vector}) \tag{29}$$

Now that all the variables of the system are solved, the movement of the system is completely understood. The mathematical model built by these two chains allows for the joint angles of the system to be analyzed through the walking and running gaits. These angles will be used for controls in later stages, but it finds an immediate use in the mechanical strength analysis of Mithra. The joint angles are used to find the wrenches of the system and give an accurate estimate of forces and moments applied to each mechanical part of the system.

3.5 Force and Stress Analyses

Finite Element Analysis was done in tandem with each step of the design phase to ensure that each part met safety factor requirements and was as light as possible. Most parts went through several manual iterations in an attempt to find the optimal weight and strength. The analysis and design were split into two main sections: ankle and knee. The ankle section of Mithra extends from the actual ankle to the knee joint, where the ankle actuators are fixed. The knee section starts at the top of the knee joint and extends through the mid-thigh, where the knee transmission is housed. The distinction between the two sections is important as design goals and necessities differ between the two.

For the ankle section of Mithra, higher safety factors were used. This section requires more durability against foot impacts. However, one benefit was that because the transmission is so light as compared to the knee, more material could be used elsewhere to ensure structural strength. Because of these factors, it was necessary to have a safety factor range of 2.5-5 for the ankle. However, with some ankle parts, such as the Main Universal Joint, the aim was to make it as strong as possible. These few and complicated parts pose a major risk to Mithra if they break, so higher safety factors were reached.

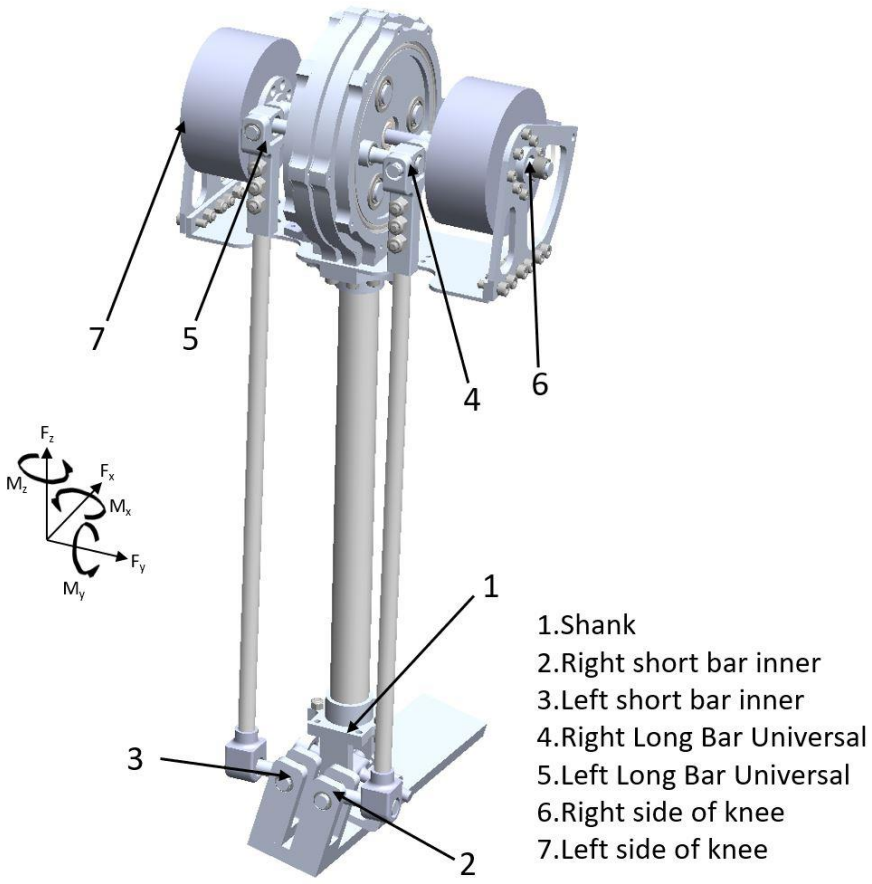

Figure 40: Force analysis reference points

The running gait data during the stance phase for ground forces and joint angles [34] were used to determine the 3D force and moments in each link of the ankle mechanism. For this purpose, a quasi-static force analysis of the whole mechanism was done, which resulted in a set of 42 equations and 42 unknowns. See Figure 40 for reference points of the analysis. Excluding the degrees of freedom, each point shown has 3 forces and 3 moments, F_x, F_y, F_z, M_x, M_y, M_z. The set of equations were solved in MATLAB, and the maximum forces through the stance phase (as shown in Figure 41),

were used for strength analyses. The maximum forces show the shank has the most force applied to it at 3500 N in the z direction.

While every part underwent finite element analysis in SolidWorks, only the most critical for each section will be discussed here. The critical ankle parts are labeled in Figure 42 and are as follows: Main Universal Joint, Shank, Main Ankle Linkage, Left-hand Side Knee Wall, Ankle Gearbox Universal Joint Yoke, Ankle Gearbox Universal Joint Main Body. These parts were defined as critical because their failure or lack of rigidity would affect the entire operation of the mechanism.

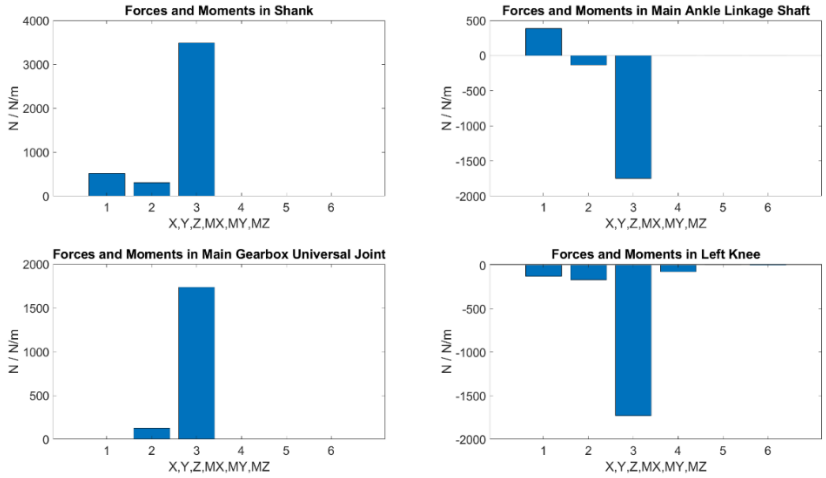

Figure 41: Forces and moments from inverse kinematics

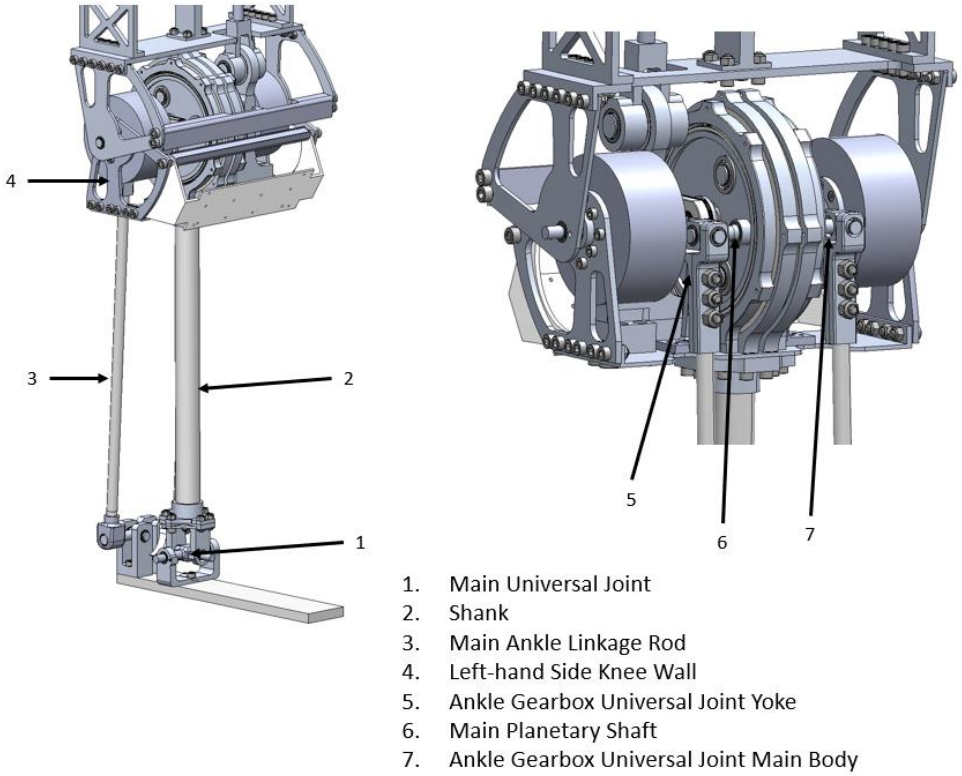

1. Main Universal Joint
2. Shank
3. Main Ankle Linkage Rod
4. Left-hand Side Knee Wall
5. Ankle Gearbox Universal Joint Yoke
6. Main Planetary Shaft
7. Ankle Gearbox Universal Joint Main Body

Figure 42: Ankle mechanism model

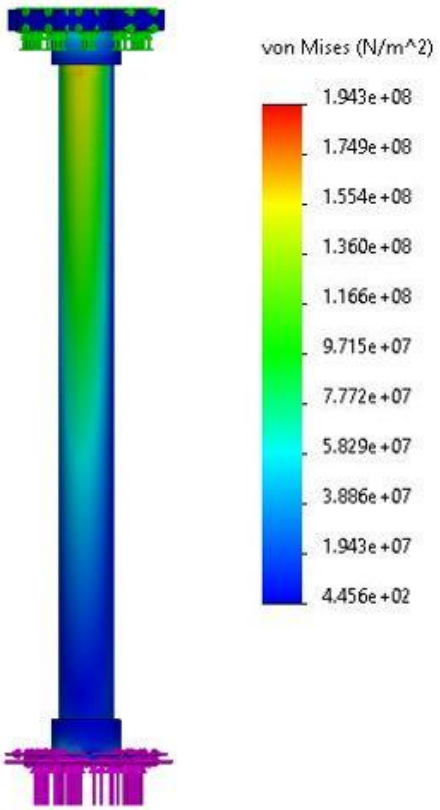

Figure 43: Shank von Mises stress plot

The shank is shown in Figure 43, with forces acting in three directions along the bottom at the ankle. 517N in the x direction, N in the 325 y direction, and 3482 N in the z direction. The top piece is fixed along the holes and surface to mimic its interaction with bolts and support plate attached to it. The maximum stress in this piece is shown to be 1.943E8 N/m^2, far below the yield strength of the carbon fiber tube, which has a tensile yield strength of 2.082E9 $N/m^{2,}$ giving this part a safety factor slightly over 10. While carbon fiber is not an isotropic material, the manufacturer tests its strengths and provides values for tensile strength and tensile modulus for each series of their tubes, allowing for analysis to verify its acceptability for the given project.

The Main Ankle Linkage is presented in Figure 44. This piece experiences a force of 500 N in the x direction, -125 in the y direction, and -1750 N in the z direction. The force in the y direction is negated by a snap ring, and the universal joint at the top is fixed. However, because the bottom connection is attached to a shaft that limits deflection, an elastic support is added. This support is equivalent to the stiffness of the rod that goes through the bearing and is calculated as below:

$$k = E\frac{A}{L} = \frac{F}{\delta} \tag{30}$$

The axial stiffness of the aluminum shaft was determined by using Equation 30, where k represents stiffness, E is the modulus, L is the length, F is the force applied, and δ is the total deflection. The shaft has a diameter of 10 mm, length of 43 mm, and a modulus of elasticity of 71.7 GPa. These values give the shaft a stiffness of 1.667E8 N/m. Using these loading conditions and fixtures, it was determined that the maximum stress on this linkage was 6.135E7 N/m^2. The pultruded carbon fiber rod has a tensile strength of 1.72E9 N/m^2, and this means the linkage has a safety factor of 28. Along with the high safety factor, the part also has high rigidity. The linkage is expected to only deflect 0.1481 mm at maximum load.

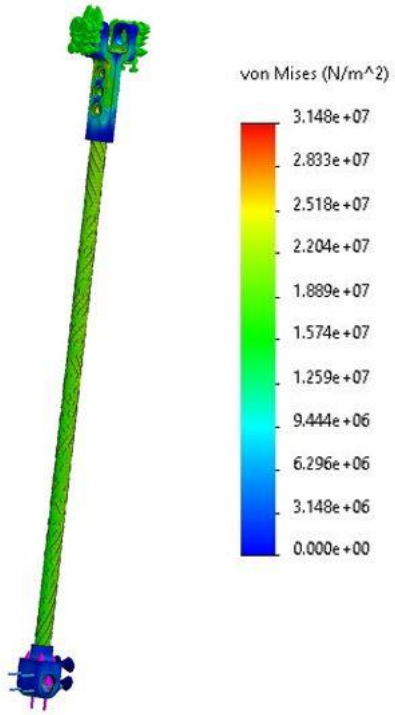

Figure 44: Main Ankle Linkage von Mises stress plot

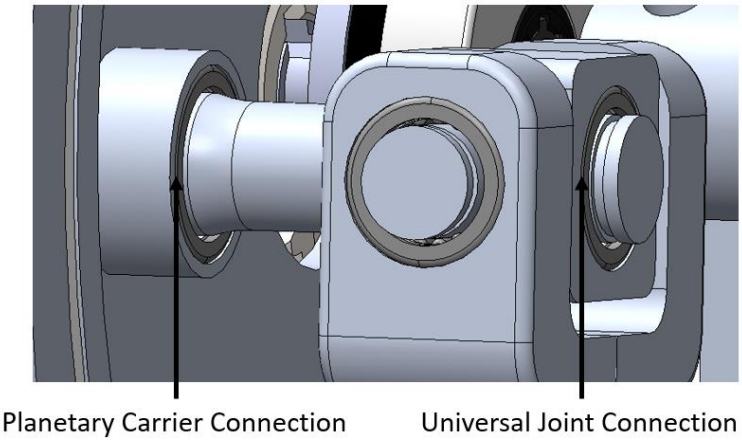

Figure 45: Main Planetary Shaft supports

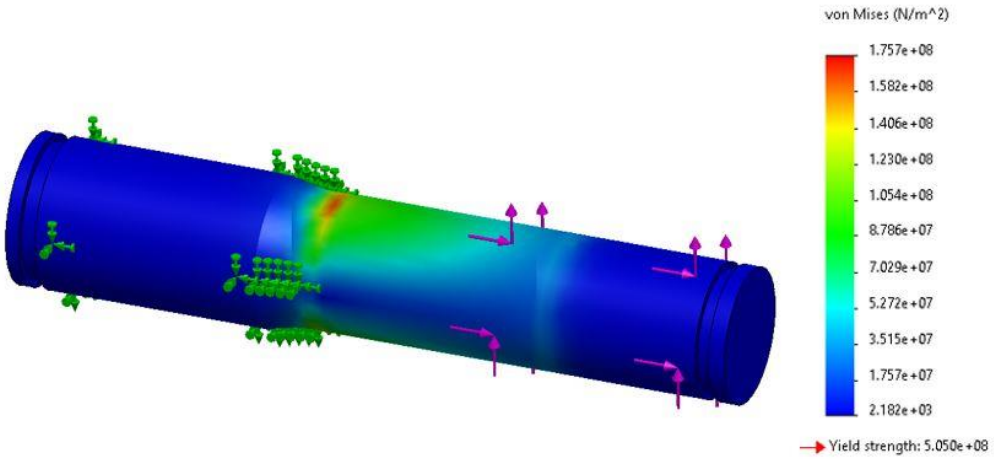

Figure 46: Main Planetary Shaft von Mises plot

The Main Planetary Shaft extended from the planetary carrier and had specific size limitations because of the gearbox size. However, it was possible to find a shaft that works through careful design of its supports. The main bearing holding in the planetary carrier extends out and is attached to a rigid linkage with a needle roller bearing. These supports are shown in Figure 45. The loading condition on this shaft is 1750 N in the y direction and 167 in the z direction. A maximum stress is seen in Figure 46 to be 1.75E8 N/m^2, leading to a safety factor of 2.88. The methods used for this analysis are optimistically constrained, and if the shaft cannot handle full running loads, it will be replaced with a much stronger and stiffer material.

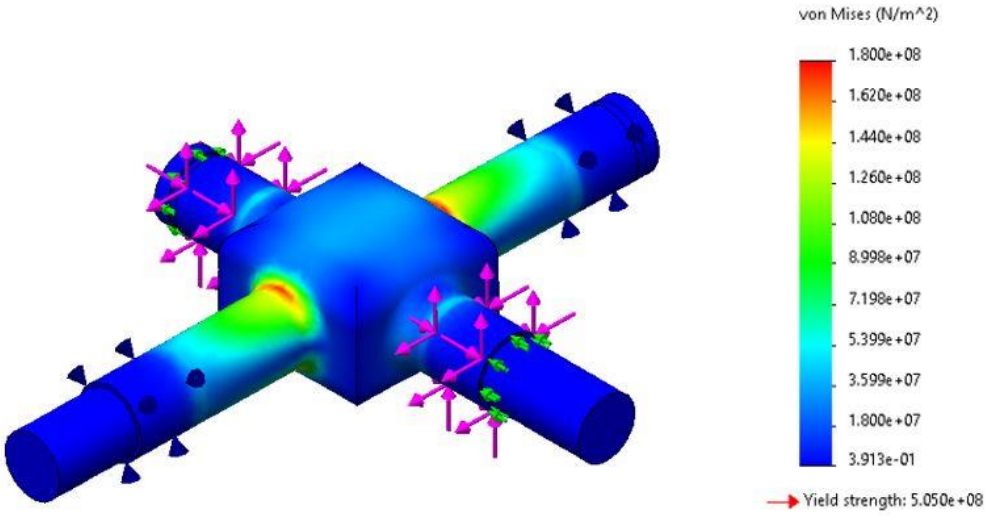

Figure 47: Main Universal Joint von Mises stress plot

The Main Universal Joint is under high load, as shown in Figure 47. The piece is well supported on every yoke with needle roller bearings and snap rings that keep it fixed axially. From the force analysis, it was determined that the maximum forces are 517 N in the x direction, 325 N in the y direction, and 3482 N in the z direction. Fixed supports were used to simulate snap rings holding the piece axially in place, and bearing connections were used where bearings are present in real life. The maximum stress on this piece is 1.8E8 N/m^2 giving it a safety factor of 2.8.

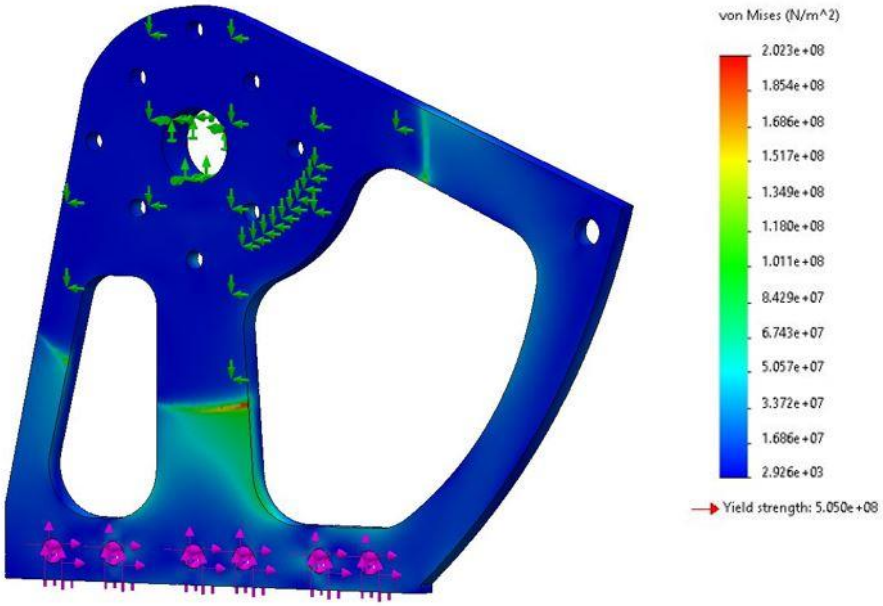

Figure 48: Left-hand Side Knee Wall von Mises stress plot

The Left-hand Side Knee Wall is shown in Figure 48, and it is identical to its counterpart on the opposite side. The loads applied to this piece are -129 N in the x direction, -167 N in the y direction, -1720 N in the z direction. It is fixed along the middle circle, as that is where its main structural support will be. The bolt holes and backside of the part are connected to the T-motor P80III, and this is represented by an on-flat faces connection on the x and z directions, replicating how it is connected to the gearbox. The maximum stress present in this part is 2.023E8 N/m^2, giving the part a safety factor of 2.5.

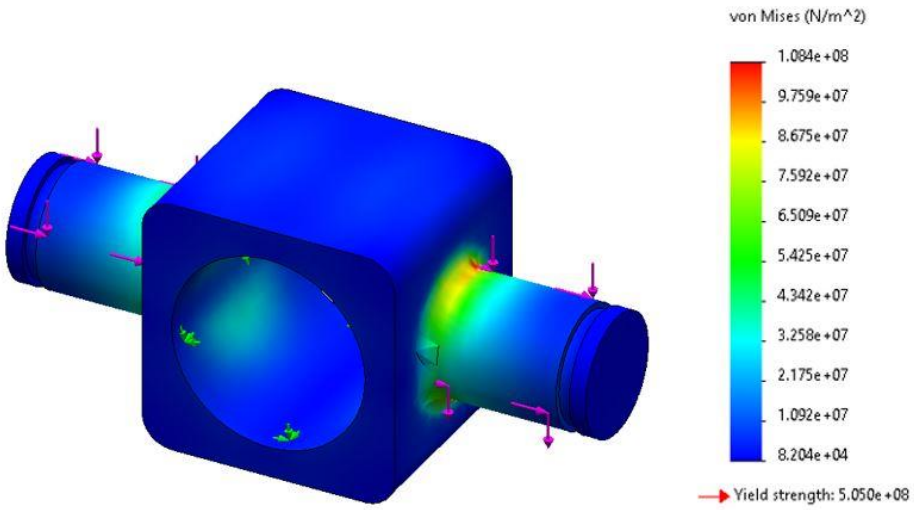

Figure 49: Ankle Gearbox Universal Joint Main Body von Mises stress plot

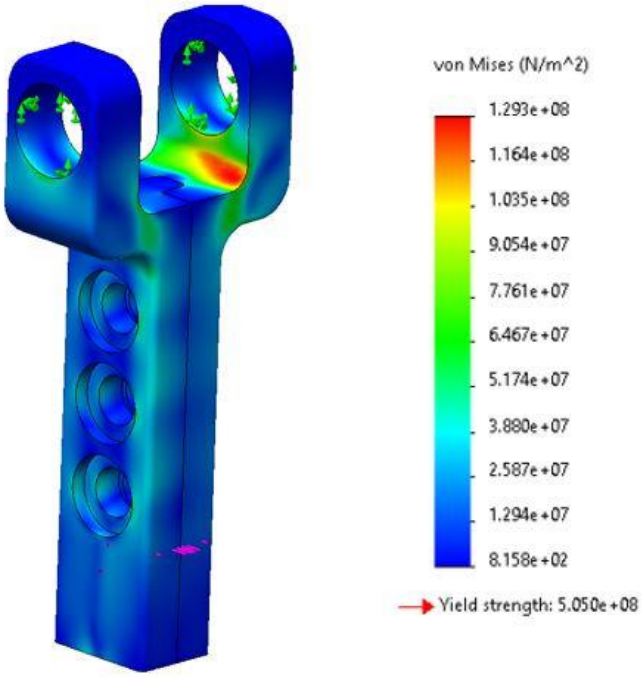

Figure 50: Ankle Gearbox Universal Joint Yoke von Mises stress plot

The Ankle Gearbox Universal Joint Yoke has two main parts pictured in Figure 49 and Figure 50. Both pieces experience the same forces as they are connected together in a serial configuration and are loaded with a sideways force in the y direction of 125 N and a vertical force in the z direction of 1750 N. For the shaft, a maximum stress of 1.084E8 N/m^2 is present at the fillet on the end of the shaft where it connects to the main body. This gives the main body a safety factor of 4.65. The yoke is loaded with the same conditions and finds a maximum stress of 1.293E8 N/m^2, giving it a safety factor of 3.9

For the knee section of Mithra, there is much less impact shock as it is located farther up the leg, so a safety factor range of 2-3.5 was used for each part. Because the strength requirements were lowered for the knee, the main focus of the analysis was to reduce the weight while maintaining rigidity. The most critical parts for the knee are labeled in Figure 51and are as follows: Knee Side Shaft Planetary Carrier, Extrusion Plate, Knee Linkage, Knee Linkage Support, and Knee Middle Support. These parts were chosen because they presented a clear risk to the manufacturability and functionality of the robot if not rigid enough.

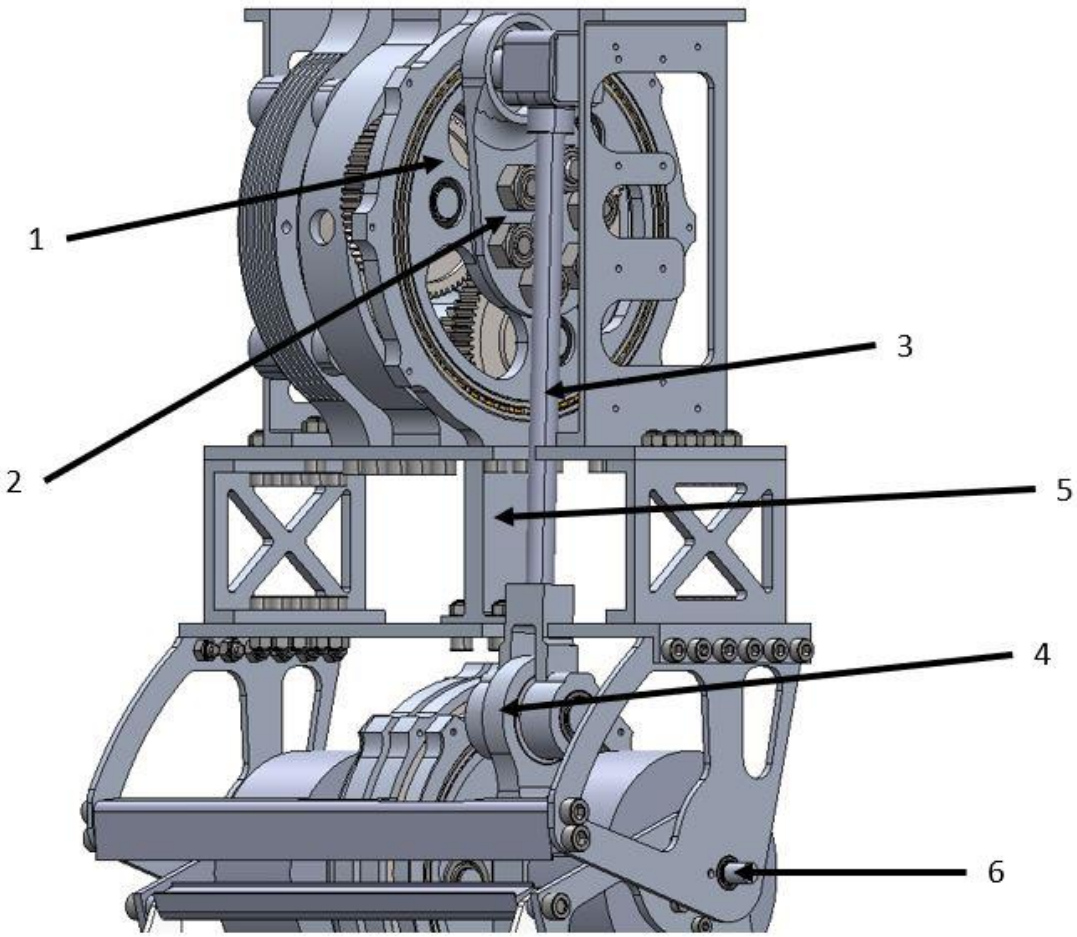

1. Planetary Carrier
2. Extrusion Plate
3. Knee Linkage
4. Knee Linkage Support
5. Knee Middle Support
6. Knee Side Shaft

Figure 51: Knee model

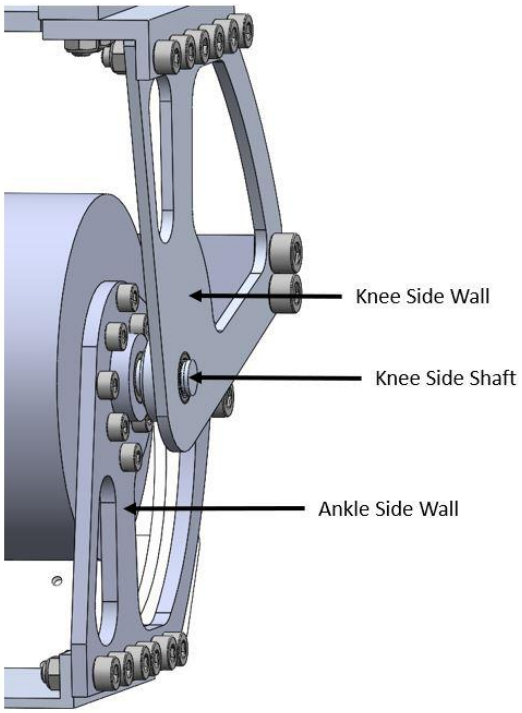

Figure 52: Side Wall model

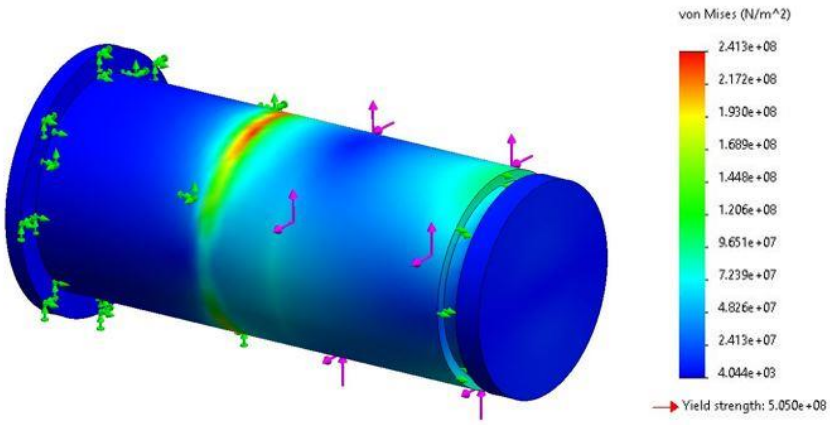

Figure 53: Knee Side Shaft von Mises stress plot

The first knee part that was designed and analyzed was the Knee Side Shaft, as seen in Figure 53. There are two of these parts on Mithra, and they connect the knee joint

to the knee actuator system above it. This part was the first knee part designed because it connects the ankle section to the knee section, as presented in Figure 52. It is loaded with the standard loading conditions seen in the ankle parts, 125 N in the y direction and 1750 N in the z direction. These loading conditions were combined with a cylindrical fixture on the left-hand side and a roller slider fixture on the right-hand side to simulate the snap ring constraint. This led to a maximum stress of 2.413E8 N/m^2, which resulted in a safety factor of 2.09.

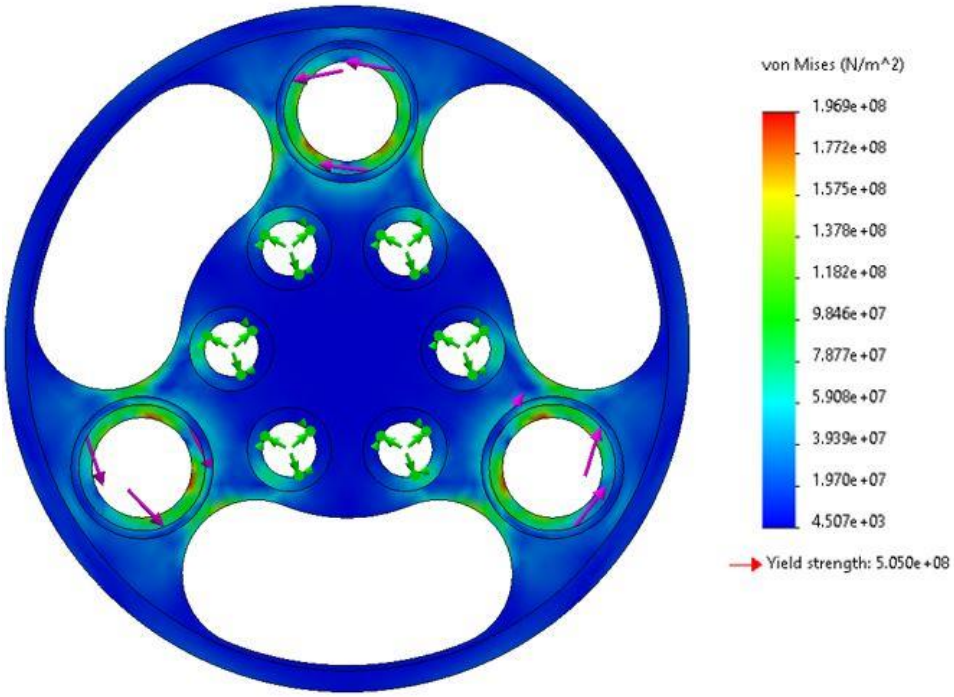

Figure 54: Knee Planetary Carrier von Mises stress plot

Shown in Figure 54 is the Knee Planetary Carrier. Each of the three large circles on the carrier is where the output of the gearbox connects to the carrier, and a torque load of 375 Nm is distributed amongst them. The pattern of six holes in the middle is where

the carrier connects to the knee linkage extrusion, and each hole is fixed on its inner cylindrical face. The analysis shows a maximum stress of 1.969E8 N/m^2 along the holes where the torque is applied, which leads to a safety factor of 2.56. This part was specifically iterated down from a much higher safety factor to remove as much weight as possible.

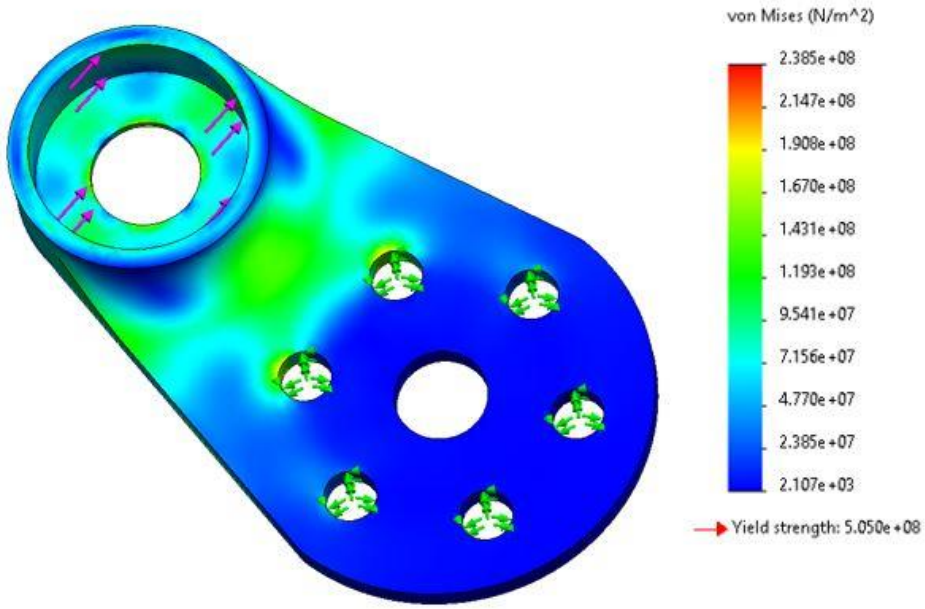

Figure 55: Knee Extrusion Plate von Mises stress plot

The Knee Extrusion Plate, as shown above in Figure 55, was loaded with a force of 3600 N perpendicular to the part in the z direction to represent the worst-case scenario. While force will be applied in many directions as the large circle is a direct connection to the knee linkage, this case represents maximum output at the worst angle for the piece. The maximum stress is seen around the uppermost bolt holes and is 1.8345E8 N/m^2. With this loading, the knee plate has a safety factor of 2.75. The deflection was examined as

well and is shown to be a maximum of .25 mm total at the far end, but this is a negligible amount for the part.

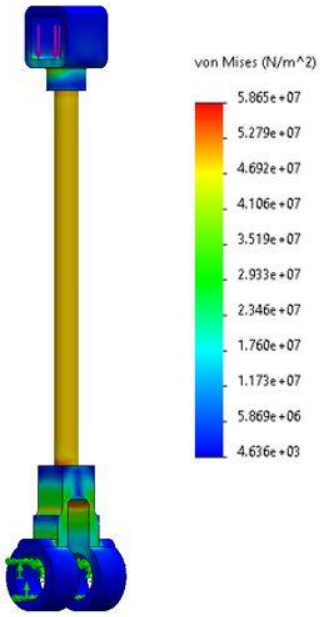

Figure 56: Knee Linkage von Mises stress plot

The Knee Linkage is pictured in Figure 56. Because of the pultruded rods' high modulus of elasticity and yield strength, it has no trouble dealing with these loads at all. The maximum stress seen on this plot is 5.865E7 N/m^2, and the yield strength of our pultruded rod in the axial direction is 1.83E9 N/m^2. This stress gives our rod a safety factor of about 31. The other pieces attached to the rod also experience the same maximum stress and are made of Al 7075, giving them a safety factor of about 8.6.

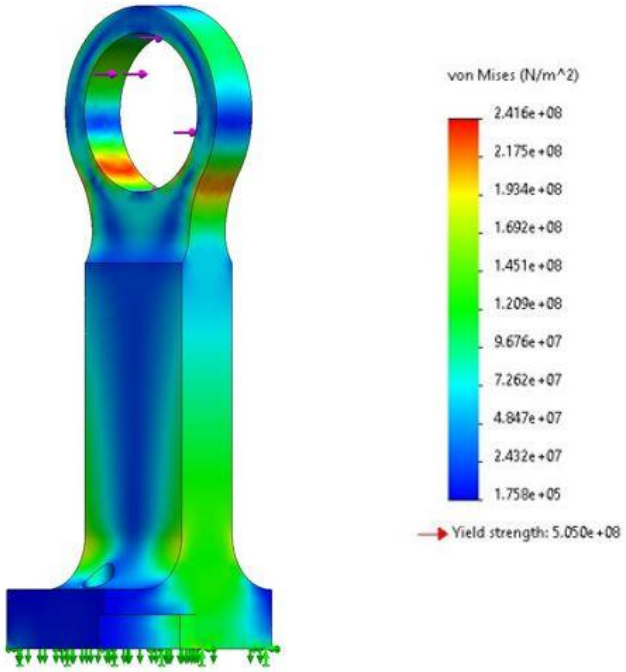

Figure 57: Knee Linkage Support von Mises stress plot

The Knee Linkage Support, pictured in Figure 57, was a vital part of the knee linkage design. This is the piece that interfaces the linkage rod with the knee joint, and it faced several limitations on the form that it could take. It was necessary that it be a certain height so that the linkage could be assembled and clear the motor and also create the correct four-bar linkage dimensions. These constraints led to a part that is taller than desired, and this height creates high stresses and deflections on this part. For this reason, it was necessary to make the part as robust as possible. During the worst-case loading condition of 3500 N exactly perpendicular to the height, a maximum stress of 2.41E8 N/m^2 is seen on the part. This gives the part a safety factor of 2.08. The maximum deflection at this angle is 1 mm, which is higher than desired but acceptable.

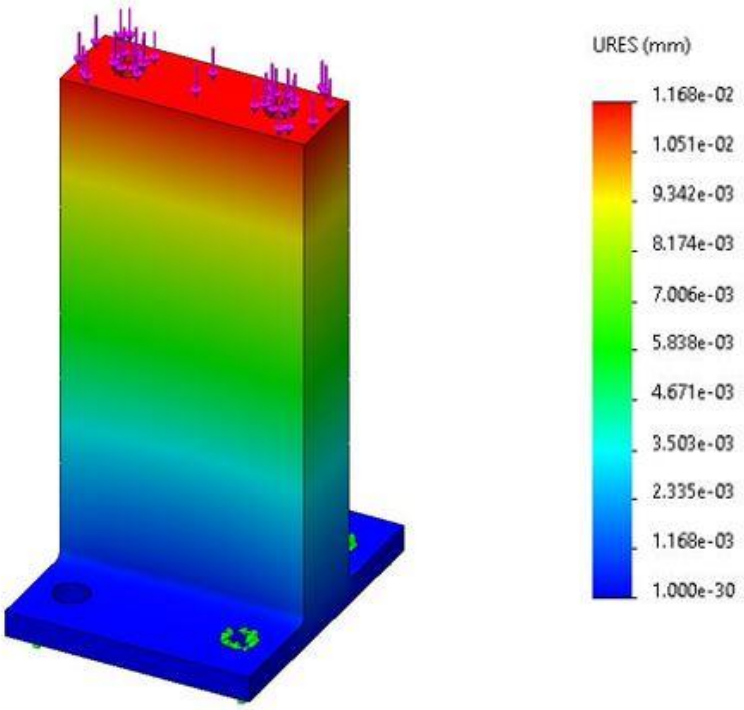

Figure 58: Knee Middle Support deflection results

While the Knee Middle Support pictured in Figure 58 is not at risk of breaking, it was immensely important that it could handle high loads with little deflection. Because of this, a value of 4000 N was placed at the top of the piece, with the bottom being fixed. The maximum deflection, in this case, is .01168 mm, which means this part is more than rigid enough to serve its purpose of supporting the knee gearbox. With this loading condition, it has a safety factor of 23; however, because it only weighs 55 grams and is midway up the thigh, it was kept at this size.

3.6 Fatigue Analysis

Fatigue life analysis was conducted using walking forces at 1.5 m/s with a safety factor of 3 and utilized a loading cycle of alternating stresses between 0 and the maximum force as ground reaction forces are in one direction only. The forces before safety factors are applied are shown in Figure 59. Walking forces were chosen as it will be the main mode of movement for Mithra will be walking and parts were chosen to be analyzed if they were candidates that met one of two criteria. They would be difficult to replace, meaning deconstruction would involve removing adhesives or take a significant amount of time. Or they were difficult to have machined, complex parts that would gain the most benefit from not being remade.

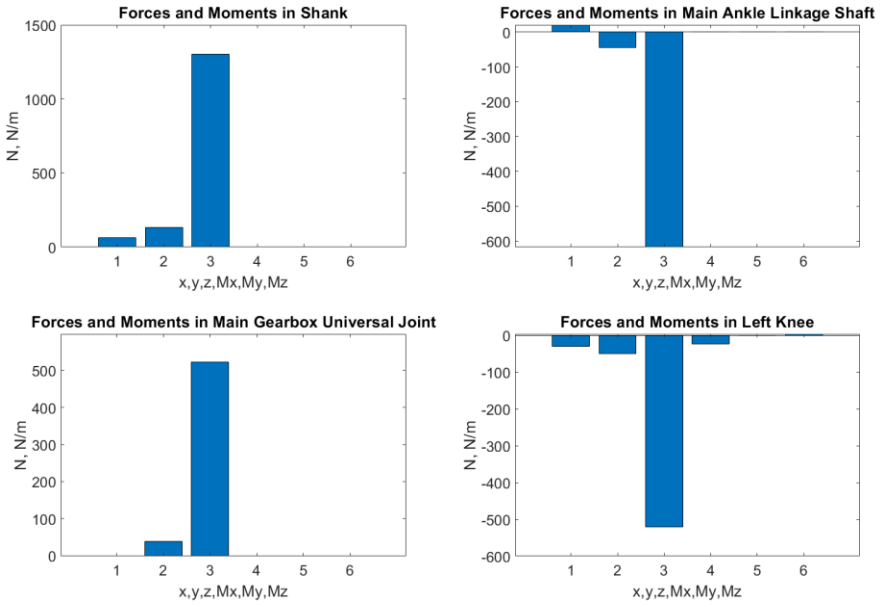

Figure 59: Peak walking forces

Al7075-T6 has excellent fatigue properties, as shown in Figure 60. Because each part was designed with a safety factor of at least 2 for running, it is expected that most

parts would have long lasting life cycles, but because of conditions not near infinite. If a part maintains an expected life lasting into 1E5 and above cycles it is considered a success.

While a fatigue life curve can be obtained for Al7075-T6 (Figure 60), it is possible to create this curve manually and account for more realistic conditions. The first detail to note for creating an S-N curve for an aluminum alloy is that the max fatigue life of 5e8 cycles typically caps out at 131 MPa [41]. For steels and other materials a value of roughly half the Ultimate strength is used to find the fatigue strength [41]. The Ultimate strength of the material can be taken as the first point, representing one cycle and ninety percent of the ultimate strength represents 1000 cycles. This assumption is only valid for bending fatigue, during axial fatigue a different number is used. Using a log-log scale the S-N curve for a fully reversed loading cycle can now be estimated. The equation of this line is dictated by the following equation:

$$S(N) = aN^b \tag{31}$$

where $S(N)$ is the fatigue strength at any N point, $a\ and\ b$ are constants that are defined by the boundary condition [41]. This method is important because it allows for the corrected fatigue strength to be calculated and plotted in the same manner. The equation for corrected fatigue strength is as follows:

$$S_f = C_{load}C_{size}C_{surf}C_{temp}C_{reliab}S_{f'} \tag{32}$$

$S_f$and S_f, are the corrected and non-corrected fatigue strength, respectively. The remaining variables in this equation represent a variety of conditions that can vary in a real system. C_{load} determines the type of load on the system, where axial loading causes greater fatigue than bending. C_{size} creates a factor that accounts for the statistical likelihood of a flaw in a larger part and C_{surf} accounts for the impact a surface finish will have on the parts overall fatigue life. C_{temp} impacts the fatigue life based on operating temperature of the material and C_{reliab} is a general gage of how reliable the part is desired to be. Using these factors, a corrected S-N curve can now be calculated using the log-log method described previously. Only the ultimate point is impacted by the corrected fatigue and the overall slope of the fatigue line is changed. The only factors that impact this system are surface and reliability, allowing us to find a corrected S_f = 90 MPa. The results can be seen in Figure 61. S-N curves allow for the number of cycles that a part will last to be calculated by estimating the alternating stress on the material. For example, if an AL7075-T6 part is under 150 MPa then using the chart in Figure 60, it can be estimated that the part would last for 1E7 cycles. On the other hand, if the part is under a load of 225 MPa then it is expected to last 1E6 cycles.

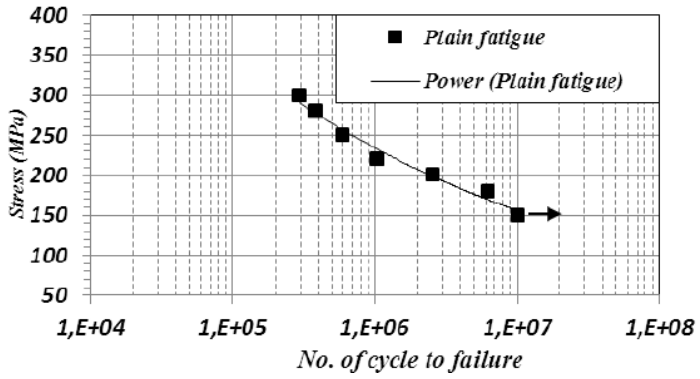

Figure 60: Fatigue life of Al7075-T6 (Figure Courtesy of Ahmed Sarhan) [42]

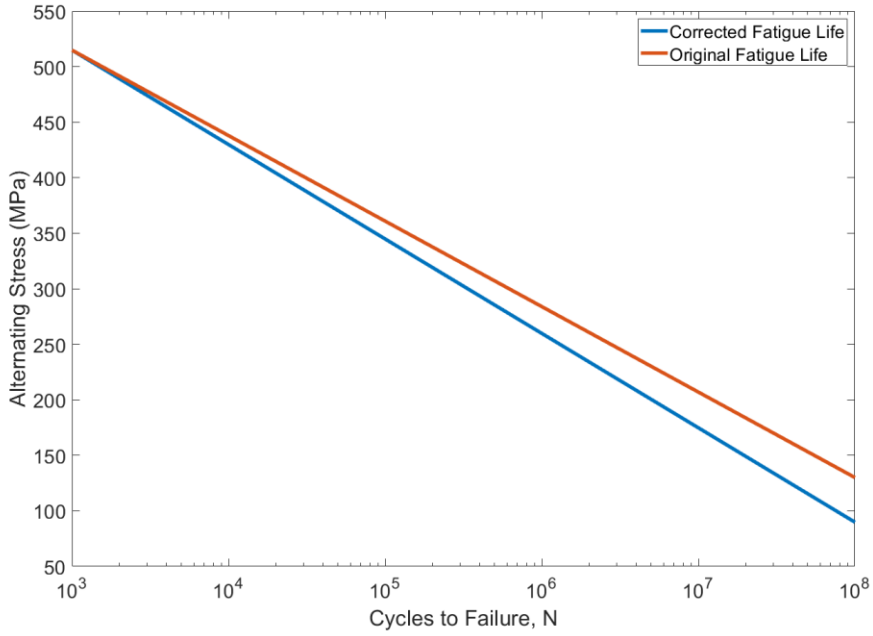

Figure 61: Calculated Fatigue Life

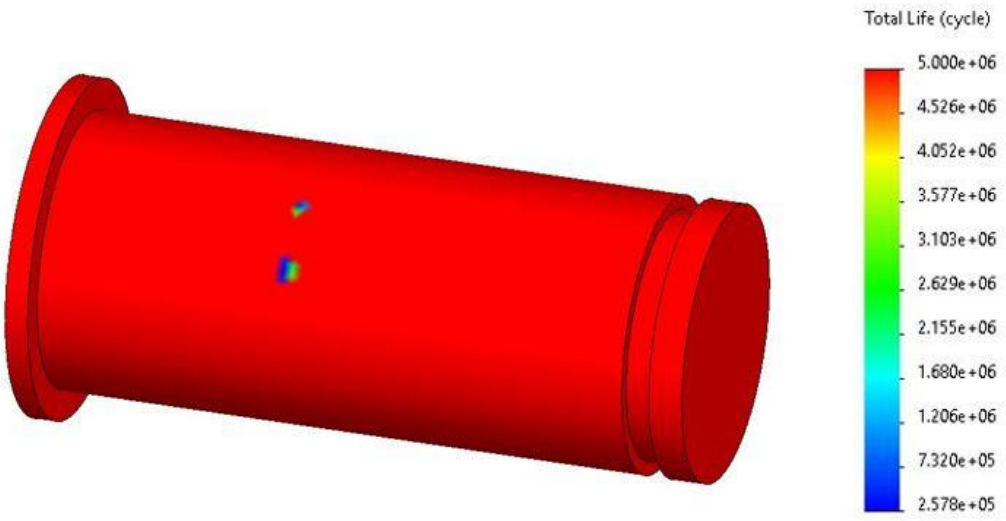

Figure 62: Fatigue life of Knee Side Shaft

Utilizing SolidWorks, several parts of Mithra were analyzed for fatigue life. The Knee Side Shaft was analyzed because it is a shaft that is not easy to replace. The ankle

gearbox is designed so that the gearbox must be disassembled, and the motor must be removed from its mount to remove this shaft. After multiplying the forces by our safety factor of 3, we find a force of 282 N in the x direction, 282 N in the y direction, and 1610 in the z direction. The resulting maximum stress for the walking forces is 2.716E8 N/m^2. The critical point on this piece is expected to last 2.578E5 cycles, and the full life cycle plot can be seen in Figure 62. This fatigue life can be verified using Equation 31. The corrected fatigue life cycle can also be calculated, providing a result of 1.225E5 cycles, roughly half of the analyzed amount.

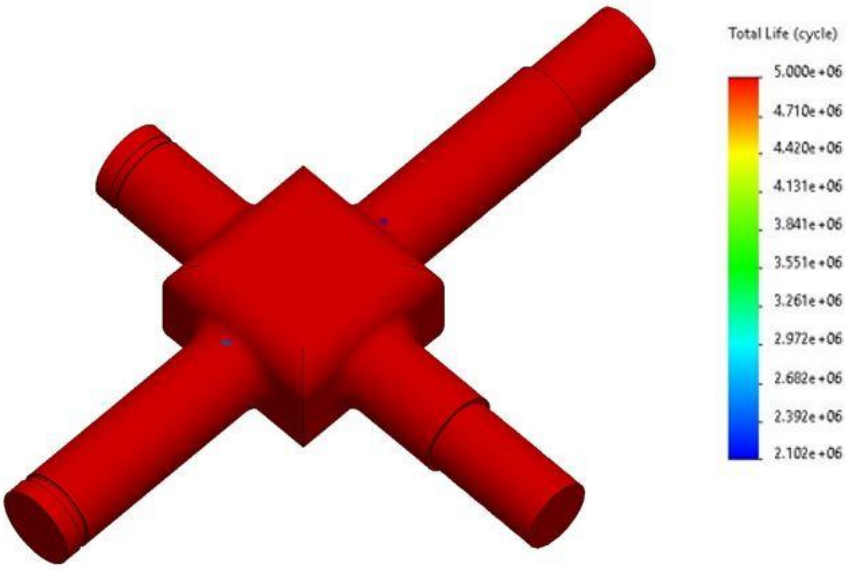

Figure 63: Main Ankle Universal Joint fatigue life cycle

The Main Ankle Universal Joint was a candidate for fatigue life analysis because of how complicated the geometry of the part is. It is without a doubt the most complicated part to manufacture on all of Mithra and deals with high loading conditions. The walking forces with a safety factor of 3 for this piece are slightly lower than the running forces, giving a load of 192 N in the x direction, 620 N in the y direction, and 4178 N in the z

direction. These forces apply a maximum stress of 2.341E8 N/m^2, which is on the S-N curve for 2.1E6 cycles. The Solidworks estimated cycle life can be seen in Figure 63. The corrected fatigue life for this part is calculated to be 4.4E5 cycles, roughly a fifth of the analyzed value.

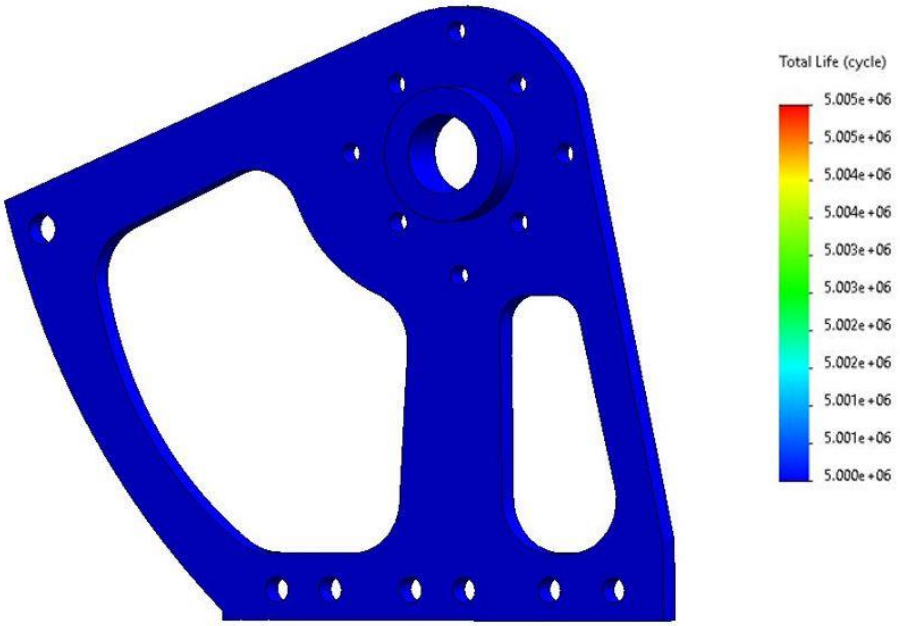

Figure 64: Fatigue life of Left-hand Side Wall

The Left-hand Side Wall was analyzed for fatigue life because it met both criteria set up earlier in the chapter. The walking forces applied are as follows: 95.1 N in the x direction, 282 N in the y direction, and 1611 N in the z direction. This resulted in a maximum stress of 2.125E8 N/m^2. Based on this, the fatigue life analysis estimates that the life cycle is 5E6 and the corrected fatigue life for this part is 8E5 cycles, again roughly a fifth of the analyze value.

After conducting fatigue life studies on several parts, it can be seen that each part should withstand loading well through the expected life cycle of Mithra. Even the parts

with the lowest corrected cyclic life of 4.4E5 cycles should still walk an estimated 880,000 feet or 167 miles with a safety factor of three. Based on the results of the analysis it can be seen that applying correction factors and developing a robust model for fatigue life is necessary to accurately analyze a design. the most likely failure condition for Mithra's parts is an unexpected shock or impact to the system.

3.7 Summary

Mithra is a humanoid robot that aims to run at 3 m/s by utilizing high-torque, low-impedance actuators along with a lightweight structure made almost entirely of Al7075-T6 and carbon fiber. Through this chapter, we have given a detailed view of the knee and ankle design for Mithra, examining the design philosophies, actuator designs, inverse kinematics, and force analysis. However, now that Mithra is built, we have insight into the decisions made along the way and data to validate the inverse kinematics of the system. In Chapter 4, we will discuss the manufacturing of Mithra, benchtop testing for ankle and knee actuators, recommendations for design improvements, and lessons learned.

Chapter Four: Results, Conclusions, and Recommendations

4.1 Benchtop Results

While the process of manufacturing Mithra presented some unexpected issues, in the end, the legs work as intended and will provide a solid mechanical testing platform. In this chapter we will cover the methods of benchtop testing and analyze the results along with discussing and diagnosing mechanical issues and room for improvements.

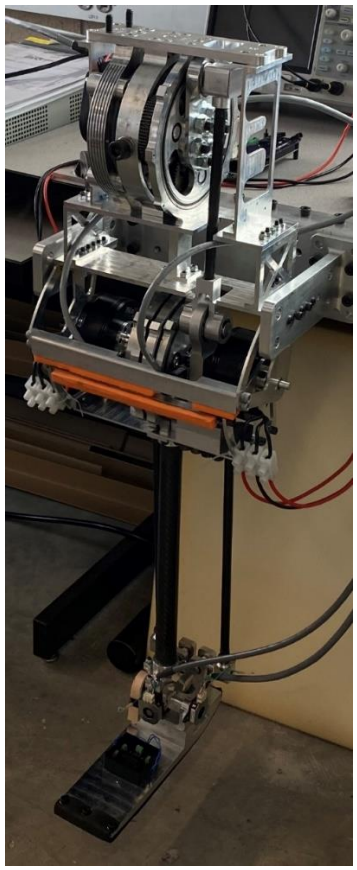

Figure 65: Mithra's left leg on testbench

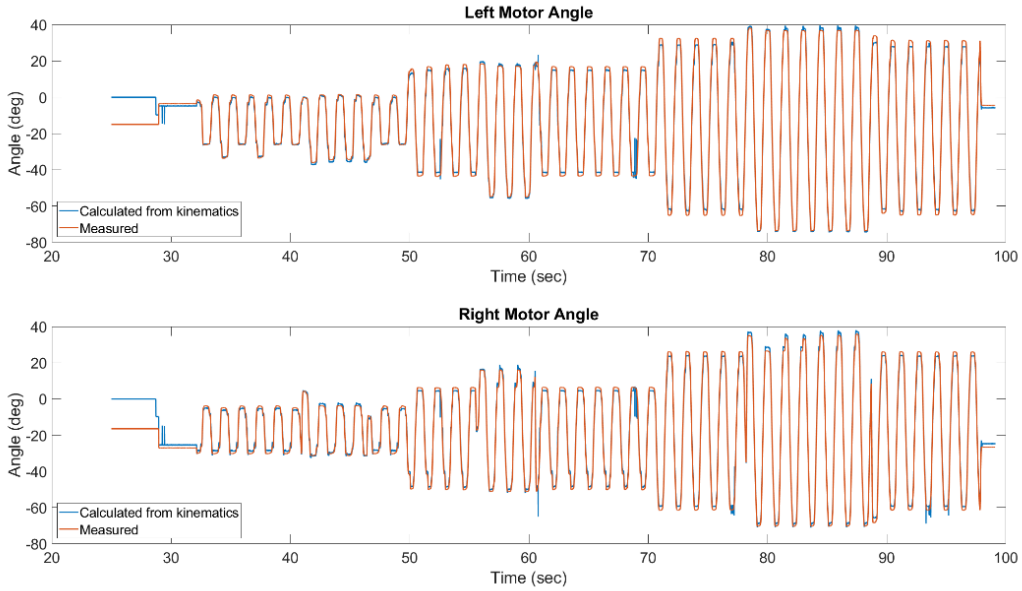

Figure 66: Left and right motor angles measured and calculated

We tested the ankle mechanism on benchtop to validate the kinematic design and analysis for the 2-DOF motions of the parallel mechanism. Because there are no encoders on the Back Ankle Universal Joint, we cannot currently validate θ_2 and θ_3 with encoder readings, but we can validate θ_1. By taking the absolute encoder readings on the Main Ankle Universal Joint we are able to calculate θ_{1l} and θ_{1r} using our inverse kinematics model, from there we divide θ_{1l} and θ_{1r} by 7 (gear ratio). The results are presented in Figure 66 and show that the model matches very closely to the measured results. The differences seen between the measured and calculated values could be caused by backlash or mechanical variations in the final build due to tolerancing.

4.2 Suggestions for Design Improvement

While Mithra is currently operational and motor testing shows that it should meet its movement goals, there are always ways to improve. This section will discuss ways that the design could be improved for rigidity, durability, and ease of manufacturing.

Manufacturing Planetary Carrier for the ankle as one piece:

this would allow for a more robust planetary carrier and rigid linkage system. The current ankle planetary carrier was designed as two pieces to save money in the manufacturing process. There is one extrusion that extends past each side of the carrier and would have increased wasted material in the machining process. However, this caused many problems in the structure of the ankle gearbox. Because of this design, glue (JB Weld) was used to hold the linkage in place, and while strong, the JB Weld is brittle and fractures easily in this position.

Changing all push-on snap rings to regular snap rings:

would increase manufacturability, precision, and rigidity of the system. Push-on snap rings have their uses; however, for the setup and building of Mithra, they do not work well. They are incredibly hard to put on and just as hard to remove. They do not work well for systems where precision is an absolute necessity.

Redesigning the absolute encoder shafts:

the current shafts that read the output of the knee joint were able to freely spin, and this was overlooked until it was manufactured. Shafts were fixed on one end

with Loctite 680 to remedy this problem. While using this glue provides a solution to the problem, it is one that could be avoided.

Redesigning the knee joint connection:

this is necessary because when the knee motor is fully stiff, there is a small amount of backlash that can be seen in the joint. This is not optimal for several reasons. The precision of the control is made less accurate by this unwanted movement and extra energy must be used to stabilize the system. One way to solve this problem is by using larger, stiffer ball bearings that connect the two pieces directly together without a shaft in between them.

Fixing the ankle gearboxes more effectively:

would enable the gearbox to have much more rigidity and thus more precise control of the ankle. The ankle gearboxes are currently fixed by two bolts on the bottom of the ring gear housing and two bolts on the planetary carrier housing. While this provides support, it is not as much as desired. Adding a second connection point would allow for a much more rigid gearbox setup, saving energy and allowing for a more robust system. There is room to connect them together at the top or connect them with bolts to the hard stop that passes in front of them.

4.3 Conclusion

This thesis presented the design and analysis of Mithra's lower legs. The aim of this design was to create an efficient, stable, and agile humanoid robotic leg system by

utilizing high-torque low-impedance actuation systems. Low-impedance designs allow for mimicking a compliant system that can mimic springs with varying stiffnesses and lead to better impedance control and efficiency. Through careful design of the actuator systems, utilizing two variations of a planetary gearbox, our designed system is expected to maintain high efficiency, remain quiet, and output high torques at fast speeds. The inverse kinematics of the ankle system were solved in order to conduct an accurate force analysis on the system and then validated through benchtop testing. These forces were utilized in the finite element analysis of all parts and the fatigue life analysis on several critical parts, ensuring strength and durability of the leg system.

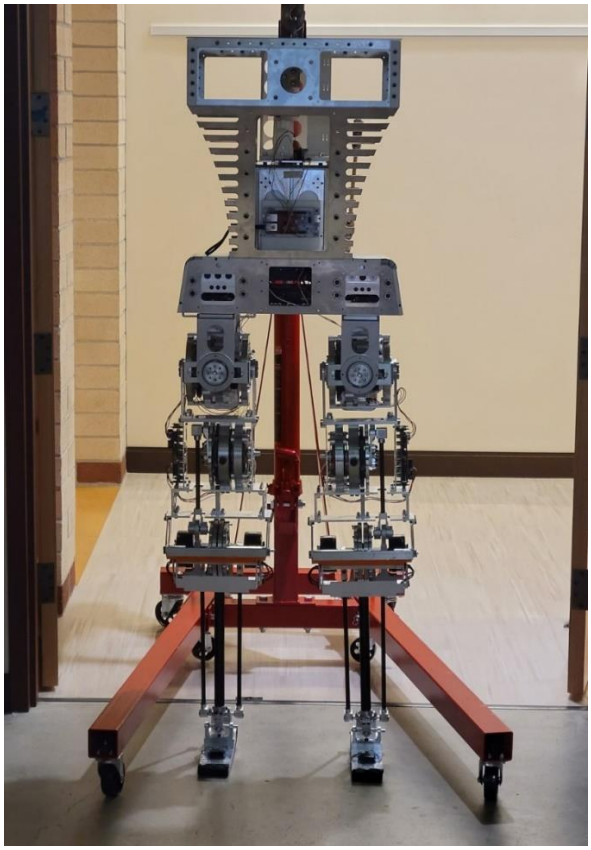

Figure 67: Mithra

While Mithra's lower limbs show precise movement and acceptable rigidity, there is still room for improvement. Higher rigidity in the joints and actuators is the biggest improvement that can currently be made. With further testing and time, the success of Mithra's design will be further understood when metrics such as power usage, stiffness, and speeds during actual walking gaits can be measured. The final build from foot to torso is pictured in Figure 67. Mithra will be used as a human movement research platform and will eventually be capable of running at 3 m/s and performing other human actions such as, walking upstairs or squatting.

References

[1] M. H. Raibert, H. B. Brown, and M. Chepponis, “Experiments in Balance with a 3D One-Legged Hopping Machine,” *Int. J. Rob. Res.*, vol. 3, no. 2, pp. 75–92, 1984, doi: 10.1177/027836498400300207.

[2] M. S. and R. H., “3D balance in legged locomotion,” *ACM SIGGRAPH Comput. Graph.*, vol. 18, no. 1, pp. 27–27, Jan. 1984, doi: 10.1145/988525.988552.

[3] M. H. Raibert *et al.*, “Stable Locomotion,” *Order A J. Theory Ordered Sets Its Appl.*, no. 4148, 1983.

[4] T. McGeer, “Passive walking with knees,” pp. 1640–1645, 1990, doi: 10.1109/ROBOT.1990.126245.

[5] C. B. Myers, “Cornell Ranger Robot Breaks New Walking Record,” *IEEE Spectrum*, 2010. https://spectrum.ieee.org/cornell-ranger-robot-breaks-new-walking-record.

[6] P. Bhounsule, J. Cortell, and A. Ruina, “Cornell ranger: Implementing energy-optimal trajectory control using low information, reflex based control Cooperative Route planning of multiple fuel-constrained Unmanned Aerial Vehicles with recharging on an Unmanned Ground Vehicle View project Cornell ,” Accessed: Oct. 14, 2021. [Online]. Available: https://www.researchgate.net/publication/277141788.

[7] C. Hubicki *et al.*, “ATRIAS: Design and validation of a tether-free 3D-capable

spring-mass bipedal robot:," *http://dx.doi.org/10.1177/0278364916648388*, vol. 35, no. 12, pp. 1497–1521, Jun. 2016, doi: 10.1177/0278364916648388.

[8] Y. Nakanishi *et al.*, "Design concept of detail musculoskeletal humanoid 'Kenshiro' - Toward a real human body musculoskeletal simulator," *IEEE-RAS Int. Conf. Humanoid Robot.*, pp. 1–6, 2012, doi: 10.1109/HUMANOIDS.2012.6651491.

[9] Y. Nakanishi *et al.*, "Design concept of detail musculoskeletal humanoid 'Kenshiro' - Toward a real human body musculoskeletal simulator," *IEEE-RAS Int. Conf. Humanoid Robot.*, pp. 1–6, 2012, doi: 10.1109/HUMANOIDS.2012.6651491.

[10] Y. Asano *et al.*, "Human mimetic musculoskeletal humanoid Kengoro toward real world physically interactive actions," *IEEE-RAS Int. Conf. Humanoid Robot.*, pp. 876–883, 2016, doi: 10.1109/HUMANOIDS.2016.7803376.

[11] S. Shigemi, *ASIMO and Humanoid Robot Research at Honda*. 2017.

[12] K. Yokoi, F. Kanehiro, K. Kaneko, S. Kajita, K. Fujiwara, and H. Hirukawa, "Experimental study of humanoid robot HRP-1S," *Int. J. Rob. Res.*, vol. 23, no. 4–5, pp. 351–362, 2004, doi: 10.1177/0278364904042194.

[13] K. Kaneko *et al.*, "Humanoid robot HRP-4 - Humanoid robotics platform with lightweight and slim body," *IEEE Int. Conf. Intell. Robot. Syst.*, pp. 4400–4407, 2011, doi: 10.1109/IROS.2011.6048074.

[14] K. Kaneko *et al.*, "Humanoid robot HRP-5P: An electrically actuated humanoid robot with high-power and wide-range joints," *IEEE Robot. Autom. Lett.*, vol. 4,

no. 2, pp. 1431–1438, 2019, doi: 10.1109/LRA.2019.2896465.

[15] O. Stasse *et al.*, “TALOS: A new humanoid research platform targeted for industrial applications,” *IEEE-RAS Int. Conf. Humanoid Robot.*, pp. 689–695, 2017, doi: 10.1109/HUMANOIDS.2017.8246947.

[16] Y. Ogura *et al.*, “Development of a new humanoid robot WABIAN-2,” *Proc. - IEEE Int. Conf. Robot. Autom.*, vol. 2006, pp. 76–81, 2006, doi: 10.1109/ROBOT.2006.1641164.

[17] A. M. M. Omer, H. Kondo, H. O. Lim, and A. Takanishi, “Development of walking support system based on dynamic simulation,” *2008 IEEE Int. Conf. Robot. Biomimetics, ROBIO 2008*, pp. 137–142, 2009, doi: 10.1109/ROBIO.2009.4912993.

[18] Y. Ogura *et al.*, “Human-like walking with knee stretched, heel-contact and toe-off motion by a humanoid robot,” *IEEE Int. Conf. Intell. Robot. Syst.*, pp. 3976–3981, 2006, doi: 10.1109/IROS.2006.281834.

[19] S. Lohmeier, *Design and Realization of a Humanoid Robot for Fast and Autonomous Bipedal Locomotion*. 2010.

[20] S. Lohmeier, T. Buschmann, and H. Ulbrich, “System design and control of anthropomorphic walking Robot LOLA,” *IEEE/ASME Trans. Mechatronics*, vol. 14, no. 6, pp. 658–666, Dec. 2009, doi: 10.1109/TMECH.2009.2032079.

[21] C. Zhou and N. Tsagarakis, “On the comprehensive kinematics analysis of a humanoid parallel ankle mechanism,” *J. Mech. Robot.*, vol. 10, no. 5, pp. 1–7, 2018, doi: 10.1115/1.4040886.

[22] G. Ficht *et al.*, “NimbRo-OP2X: Adult-Sized Open-Source 3D Printed Humanoid Robot,” *IEEE-RAS Int. Conf. Humanoid Robot.*, vol. 2018-Novem, pp. 747–754, 2019, doi: 10.1109/HUMANOIDS.2018.8625038.

[23] G. Ficht, P. Allgeuer, H. Farazi, and S. Behnke, “NimbRo-OP2: Grown-up 3D printed open humanoid platform for research,” *IEEE-RAS Int. Conf. Humanoid Robot.*, pp. 669–675, 2017, doi: 10.1109/HUMANOIDS.2017.8246944.

[24] E. Guizzo, “How Boston Dynamics is redefining Robot Agility,” *IEEE Spectrum*, 2021. .

[25] G. Ficht and S. Behnke, “Bipedal Humanoid Hardware Design: a Technology Review,” *Curr. Robot. Reports*, vol. 2, no. 2, pp. 201–210, 2021, doi: 10.1007/s43154-021-00050-9.

[26] D. A. Winter, *Biomechanics and Motor Control of Human Movement: Fourth Edition*. 2009.

[27] B. Morris and J. W. Grizzle, “Hybrid Invariance in Bipedal Robots with Series Compliant Actuators.”

[28] S. Seok *et al.*, “Design principles for energy-efficient legged locomotion and implementation on the MIT Cheetah robot,” *IEEE/ASME Trans. Mechatronics*, vol. 20, no. 3, pp. 1117–1129, Jun. 2015, doi: 10.1109/TMECH.2014.2339013.

[29] T. Apgar, P. Clary, K. Green, A. Fern, and J. Hurst, “Fast Online Trajectory Optimization for the Bipedal Robot Cassie.”

[30] T. Elery, S. Rezazadeh, C. Nesler, and R. D. Gregg, “Design and validation of a powered knee-ankle prosthesis with high-torque, low-impedance actuators,” *IEEE*

Trans. Robot., vol. 36, no. 6, pp. 1649–1668, 2020, doi: 10.1109/TRO.2020.3005533.

[31] P. M. Wensing, A. Wang, S. Seok, D. Otten, J. Lang, and S. Kim, "Proprioceptive actuator design in the MIT cheetah: Impact mitigation and high-bandwidth physical interaction for dynamic legged robots," *IEEE Trans. Robot.*, vol. 33, no. 3, pp. 509–522, Jun. 2017, doi: 10.1109/TRO.2016.2640183.

[32] C. Semasinghe, D. Taylor, and S. Rezazadeh, "A More Effective Set of Performance Metrics for Robot Leg Design through a Unified Optimization Framework," vol. 1, no. Icra, pp. 4919–4925, 2020.

[33] M. Wisse, A. L. Schwab, R. Q. van der Linde, and F. C. T. van der Helm, "How to keep from falling forward: Elementary swing leg action for passive dynamic walkers," *IEEE Trans. Robot.*, vol. 21, no. 3, pp. 393–401, Jun. 2005, doi: 10.1109/TRO.2004.838030.

[34] J. Wojtusch and O. Von Stryk, "HuMoD - A versatile and open database for the investigation, modeling and simulation of human motion dynamics on actuation level," *IEEE-RAS Int. Conf. Humanoid Robot.*, vol. 2015-Decem, pp. 74–79, 2015, doi: 10.1109/HUMANOIDS.2015.7363534.

[35] "Aluminum 7075-T6; 7075-T651." http://www.matweb.com/search/DataSheet.aspx?MatGUID=4f19a42be94546b686bbf43f79c51b7d (accessed Oct. 17, 2021).

[36] "Titanium Ti-6Al-4V (Grade 5), Annealed Bar." http://www.matweb.com/search/DataSheet.aspx?MatGUID=10d463eb3d3d4ff48fc

57e0ad1037434 (accessed Oct. 17, 2021).

[37] "AISI 4140 Steel, oil quenched, 100 mm (4 in.) round [845°C (1550°F) quench, 540°C (1000°F) temper]." http://www.matweb.com/search/DataSheet.aspx?MatGUID=9f4b2e94285d46ecb679151a4aeb91d2&ckck=1 (accessed Oct. 17, 2021).

[38] "Aluminum 6061-T6; 6061-T651." http://www.matweb.com/search/datasheet_print.aspx?matguid=1b8c06d0ca7c456694c7777d9e10be5b (accessed Oct. 17, 2021).

[39] E. Of and M. Gear, "Formulas Diversas."

[40] M. V. Mark Spong, Seth Hutchinson, *Robot Modeling and Control*. John Wiley & Sons, Ltd, 2006.

[41] R. L. Norton, *Machine Design: An Integrated Approach (4th Edition)*. 2011.

[42] E. Zalnezhad, D. Ahmed, A. Sarhan, M. Abd Shukor, and B. Asri, "A Fuzzy Logic Based Model to Predict the Fretting Fatigue Life of Aerospace Al7075-T6 Alloy," vol. 1, pp. 39–48, 2012.

Appendix A

```
clear all; clc;
RingGear   = [80 90 96 100 110 120];  %Ring Gear Choices from Vendors
RingPlanet = [14 15 16 17 18 19 20 21 22 23 24 25 26 27 28 29 30 32 34
35 36 38 40]; %Ring Planet Choices
PlanetSun  = [36 38 40 42 44 45 48 50 55 56 60 64 65 70 75 80 85 90];
%Planet Sun Choices
Sun        = [16 17 18 19 20 21 22 23 24 25 26 27 28 29 30 32 34 35 36
38 40]; % Sun Choices
ModuleA = 1; %Module of Ring Gear and Ring Planet ( Different Modules
can be Mixed,but only between non meshing gears. That is why there is
an A and B)
ModuleB = 1;   %Module of Sun and Sun Planet
[X,Y,Z] = meshgrid(RingPlanet,PlanetSun,Sun);

%Decide which Ring Gear to use. Determines size.
RingGear = [120]; %(Choosing the starting ring gear makes this script
run)
for i = 1:7000; %If original gear matrices are lengthened then this
must be made larger as well.
    if ModuleA*RingGear - ModuleA*X(i) - ModuleB*Y(i) - ModuleB*Z(i) ==
0  %Determine if gears fit together. Defining equation for planetary
system
       GearRatio{i}= 1 + (RingGear*Y(i))/ (X(i)*Z(i));
    else GearRatio{i}=0;
       %i= i +1;
    end
end
C = cell2mat(GearRatio);
B = C(C~=0)
[row,col] = find(C>14.5& C<15.4,6) %Input Gear Ratio you want here.
Please note you need to go slightly larger than what you would want. If
you are looking for a ratio of 14 you need to make the upper bounds at
least 14.1
%The answer will come out in a matrix with RingPlanet, PlanetSun, Sun
X(col),Y(col),Z(col)
 1 + (RingGear*Y(col(1)))/ (X(col(1))*Z(col(1))) %The Gear ratio of the
corresponding configuration.
 1 + (RingGear*Y(col(2)))/ (X(col(2))*Z(col(2)))
 1 + (RingGear*Y(col(3)))/ (X(col(3))*Z(col(3)))
 1 + (RingGear*Y(col(4)))/ (X(col(4))*Z(col(4)))
 1 + (RingGear*Y(col(5)))/ (X(col(5))*Z(col(5)))
 1 + (RingGear*Y(col(6)))/ (X(col(6))*Z(col(6)))
```